



HAL
open science

Magnetocaloric effect and slow magnetic relaxation in peroxide-assisted tetranuclear lanthanide assemblies

Pawan Kumar, Jessica Flores Gonzalez, Prem Prakash Sahu, Naushad Ahmed, Joydev Acharya, Vierandra Kumar, Olivier Cador, Fabrice Pointillart, Saurabh Kumar Singh, Vadapalli Chandrasekhar

► **To cite this version:**

Pawan Kumar, Jessica Flores Gonzalez, Prem Prakash Sahu, Naushad Ahmed, Joydev Acharya, et al.. Magnetocaloric effect and slow magnetic relaxation in peroxide-assisted tetranuclear lanthanide assemblies. *Inorganic Chemistry Frontiers*, 2022, 9 (19), pp.5072-5092. 10.1039/D2QI01260J . hal-04008243

HAL Id: hal-04008243

<https://univ-rennes.hal.science/hal-04008243v1>

Submitted on 1 Mar 2023

HAL is a multi-disciplinary open access archive for the deposit and dissemination of scientific research documents, whether they are published or not. The documents may come from teaching and research institutions in France or abroad, or from public or private research centers.

L'archive ouverte pluridisciplinaire **HAL**, est destinée au dépôt et à la diffusion de documents scientifiques de niveau recherche, publiés ou non, émanant des établissements d'enseignement et de recherche français ou étrangers, des laboratoires publics ou privés.

Magneto Caloric Effect and Slow Magnetic Relaxation in Peroxide-assisted Tetranuclear Lanthanide Assemblies

Pawan Kumar,^a Jessica Flores Gonzalez,^b Prem Prakash Sahu,^{c‡} Naushad Ahmed,^{d‡} Joydev Acharya,^a Vierandra Kumar,^a Olivier Cador,^b Fabrice Pointillart,^{*b} Saurabh Kumar Singh^{*c} and Vadapalli Chandrasekhar^{* a,d}

^a Department of Chemistry, Indian Institute of Technology Kanpur, Kanpur-208016, India

^b Univ Rennes, CNRS, ISCR (Institut des Sciences Chimiques de Rennes) - UMR 6226, 35000 Rennes, France

^c Department of Chemistry, Indian Institute of Technology Hyderabad, Kandi, Sangareddy, Telangana-502285, India

^d Tata Institute of Fundamental Research Hyderabad, Gopanpally, Hyderabad-500046, Telangana, India

[‡] Authors contributed equally

Abstract

The synthesis, structure and magnetism of tetranuclear complexes, $[\text{Ln}_4(\text{LH}_2)_2(\eta^1\text{-Piv})_2(\eta^2\text{-Piv})_2(\mu_3\text{-O}_2)_2(\text{H}_2\text{O})_2] \cdot 2\text{MeOH}$ (**1**, Ln = Gd^{III}; **2**, Ln = Tb^{III}; **3**, Ln = Dy^{III}; **4**, Ln = Er^{III}) (LH₄ = 6-((bis(2-hydroxyethyl)amino)-*N'*-(2-hydroxybenzylidene)picolinohydrazide), (piv = pivalate ion) are reported. Interestingly, the formation of these tetranuclear assemblies is assisted by two side-on coordinating peroxide ligands which bind in a $\mu_3\text{-}\eta^2:\eta^2:\eta^2$ fashion. DC magnetic behaviour revealed the existence of a dominating but weak intramolecular antiferromagnetic interaction in the cases of **1**, **2**, and **4** while a small structural change in complex **3** turns this into a ferromagnetic interaction. We have investigated the magnetothermal behaviour of **1** which shows

a magnetocaloric effect with the value of maximum entropy change of $-\Delta S_m = 33.60 \text{ J K}^{-1} \text{ Kg}^{-1}$ at 4 K ($\Delta H = 13.0 \text{ T}$). This is close to the calculated value of $36.45 \text{ J K}^{-1} \text{ Kg}^{-1}$. The ac magnetic susceptibility study confirms zero-field out-of-phase magnetic susceptibility signals only for **3** which get well resolved on the application of 1 kOe dc magnetic field. The energy barrier for the Orbach process of spin reversal was found to be 23 K ($\tau_0 = 9 \times 10^{-7} \text{ s}$). We also report detailed theoretical studies to rationalize and understand the observed magnetic behaviour.

Introduction

Lanthanide complexes have attracted considerable attention in recent years in the field of catalysis,¹⁻³ molecular magnets⁴⁻⁸ as well as photophysical properties.^{9, 10} The use of lanthanide complexes in molecular magnetism in general and single-molecule magnets (SMMs) in particular has been triggered by the seminal discovery of Ishikawa in 2003 that the complex $[\text{Bu}_4\text{N}][\text{TbPc}_2]$ showed a blocking of magnetization below a critical temperature.¹¹ The intrinsic high spin of many lanthanide ions and their strong spin-orbit coupling make them attractive candidates for assembling single-molecule magnets.¹²⁻²¹ Another aspect of interest in lanthanide complexes is molecular refrigeration which can be generated by the so-called magnetocaloric effect (MCE). It has been shown that MCE can be maximized by the presence of metal ions that can contribute to a high spin and have negligible anisotropy.²²⁻²⁹ These criteria are fulfilled quite nicely by Gd^{III} and not surprisingly many Gd^{III} complexes have been investigated for their MCE.³⁰⁻⁴³ An additional caveat among polynuclear Gd^{III} complexes for displaying MCE is the presence of weak ferromagnetic coupling between the Gd^{III} centres.

We have been working on the design of multinuclear Ln^{III} complexes for some time now. We have extensively used aroylhydrazone Schiff base ligands for this purpose. These ligands have

many favourable features including flexible coordination pockets, C-C/C-N/N-N bond rotation as well as keto-enol tautomerization (vide infra).⁴⁴⁻⁵⁰ In this context, recently we have utilized this family of ligands along with an aryl phosphonate, $[\text{RPO}_3]^{2-}$, to assemble a tetranuclear ensemble (vide infra).⁴⁹ The phosphonate ligand helps in connecting the two dinuclear motifs together to afford the tetranuclear complex. In view of the large number of transition metal complexes containing the peroxide ligand, we were intrigued to investigate the effect of peroxide as a co-ligand along with the aroylhydrazone Schiff base ligand in lanthanide chemistry. We reasoned that in its *side-on* coordinating mode the peroxide ligand would function akin to the phosphonate ligand and help in assembling a tetranuclear complex. Accordingly, we report the synthesis, structural characterization, and magnetic studies of the peroxide-containing tetranuclear assemblies, $\text{Ln}_4(\text{LH}_2)_2(\eta^1\text{-Piv})_2(\eta^2\text{-Piv})_2(\mu_3\text{-O}_2)_2(\text{H}_2\text{O})_2] \cdot 2\text{MeOH}$ {where $\text{Ln} = \text{Gd}^{\text{III}}$ (**1**), Tb^{III} (**2**), Dy^{III} (**3**), Er^{III} (**4**)}. As anticipated, the peroxide ligand binds in a *side-on* $\mu_3\text{-}\eta^2:\eta^2:\eta^2$ fashion.

Experimental Section

Solvents and other general reagents used in this work were purified according to standard procedures.⁵¹⁻⁵² Pyridine-2,6-dicarboxylic acid, sodium borohydride, H_2O_2 (34.5-36.5% w/v), $\text{DyCl}_3 \cdot 6\text{H}_2\text{O}$, $\text{TbCl}_3 \cdot 6\text{H}_2\text{O}$, $\text{ErCl}_3 \cdot 6\text{H}_2\text{O}$, and $\text{GdCl}_3 \cdot 6\text{H}_2\text{O}$ were obtained from Sigma Aldrich Chemical Co. and were used as received. Diethanolamine, hydrazine hydrate (80%), PBr_3 , and sodium sulphate (anhydrous) were obtained from S.D. Fine Chemicals, Mumbai, India. Methyl-6-(hydroxymethyl) picolinate, methyl 6-(bromomethyl)picolinate,⁵³ methyl-6-((bis(2-hydroxyethyl) amine)methyl)picolinate,⁴⁷ and 6-((bis(2-hydroxyethyl)amino)methyl)picolinohydrazide,⁴⁷ were prepared according to literature procedures.

Instrumentation

Melting points were measured on a JSGW melting point apparatus and are reported uncorrected. IR spectra were recorded as KBr pellets on a Bruker Vector 22 FT IR spectrophotometer operating at 400–4000 cm^{-1} . Elemental analyses of the compounds were obtained from Thermoquest CE instruments CHNS-O, E.A./110 model. ESI-MS spectra were recorded on a MICROMASS QUATTRO II triple quadrupole mass spectrometer. ^1H NMR spectra were recorded in CDCl_3 and DMSO-d^6 solutions on a JEOL JNM LAMBDA 400 model spectrometer operating at 500.0 MHz. Chemical shifts are reported in parts per million (ppm) and are referenced with respect to internal tetramethylsilane (^1H). Powder X-ray diffraction study was performed on finely ground polycrystalline material with Bruker D8 Advance Powder X-ray diffractometer.

X-ray Crystallography

Single crystal data for all the complexes were collected on a Bruker *SMART* CCD diffractometer (MoK_α radiation, $\lambda = 0.71073 \text{ \AA}$). The program *SMART*⁵⁴ was used for collecting frames of data, indexing reflections, and determining lattice parameters, *SAINTE* for integration of the intensity of reflections and scaling, *SADABS*⁵⁵ for absorption correction, and *SHELXTL*⁵⁶ for space group and structure determination and least-squares refinements on F^2 . The crystal structures were solved and refined by full-matrix least-squares methods against F^2 by using the program *SHELXL-2014*⁵⁷ using *Olex-2*⁵⁸ software. All the non-hydrogen atoms were refined with anisotropic displacement parameters. Hydrogen atoms were fixed at calculated positions and refined isotropically. The crystallographic figures have been generated using *Diamond 3.1e*

software.⁵⁹ The crystal data, CCDC information, and cell parameters for the complexes **1-4** are summarized in Table 1.

Table 1. Crystal data and structure refinement parameters of complexes **1-4**

	1	2	3	4
Formula	C ₅₈ H ₈₈ Gd ₄ N ₈ O ₂₄	C ₅₈ H ₈₈ N ₈ Tb ₄ O ₂₄	C ₅₈ H ₈₈ Dy ₄ N ₈ O ₂₄	C ₅₈ H ₈₈ Er ₄ N ₈ O ₂₄
g/mol	1910.36	1917.04	1931.36	1950.40
Crystal system	Triclinic	Triclinic	Triclinic	Monoclinic
Space group	<i>P</i> -1	<i>P</i> -1	<i>P</i> -1	<i>P</i> -1
<i>a</i>/Å	10.862(10)	10.809(11)	10.800(5)	10.830(5)
<i>b</i>/Å	13.136(12)	13.071(13)	13.061(5)	13.029(5)
<i>c</i>/Å	13.290(12)	13.263(14)	13.350(5)	13.579(5)
α (°)	94.270(2)	94.202(3)	94.576(5)	96.466(5)
β (°)	102.678(2)	102.719(3)	102.765(5)	103.556(5)
γ (°)	110.320(2)	110.284(3)	110.248(5)	109.626(5)
<i>V</i>/Å³	1711.5(3)	1691.6(3)	1697.8(12)	1715.7(12)
<i>Z</i>	1	1	1	1
ρ/g cm⁻³	1.854	1.882	1.889	1.888
μ/mm⁻¹	3.907	4.212	4.433	4.923
<i>F</i>(000)	940.0	944.0	948.0	956.0
Cryst size (mm³)	0.12 × 0.09 × 0.07	0.15 × 0.012 × 0.09	0.15 × 0.13 × 0.06	0.14 × 0.11 × 0.07
2θ range (deg)	5.62 to 50.278	5.646 to 50.166	5.012 to 50.22	5.608 to 50.998
Limiting indices	-12 ≤ <i>h</i> ≤ 12 -15 ≤ <i>k</i> ≤ 15 -15 ≤ <i>l</i> ≤ 15	-12 ≤ <i>h</i> ≤ 12 -15 ≤ <i>k</i> ≤ 15 -15 ≤ <i>l</i> ≤ 15	-12 ≤ <i>h</i> ≤ 12 -15 ≤ <i>k</i> ≤ 15 -15 ≤ <i>l</i> ≤ 15	-13 ≤ <i>h</i> ≤ 13 -15 ≤ <i>k</i> ≤ 15 -16 ≤ <i>l</i> ≤ 16
Reflns collected	20397	19819	17978	20945
Ind reflns	6105 [<i>R</i> (int) = 0.0434]	5992 [<i>R</i> (int) = 0.0572]	6041 [<i>R</i> (int) = 0.0493]	6366 [<i>R</i> (int) = 0.0425]
Completeness to θ (%)	100	100	100	100
Refinement method	Full-matrix least-squares on <i>F</i> ²	Full-matrix least-squares on <i>F</i> ²	Full-matrix least-squares on <i>F</i> ²	Full-matrix least-squares on <i>F</i> ²
Data/restraints/params	6105/6/439	5992/6/439	6041/6/439	6366/15/403

Goodness -of-fit on F^2	1.041	1.020	1.053	1.052
Final R indices [$I >$ $2\theta(I)$]	$R_1 = 0.0300$ $wR_2 = 0.0645$	$R_1 = 0.0423$ $wR_2 = 0.0801$	$R_1 = 0.0372$ $wR_2 = 0.0756$	$R_1 = 0.0434$ $wR_2 = 0.0948$
R indices (all data)	$R_1 = 0.0438$ $wR_2 = 0.0690$	$R_1 = 0.0692$ $wR_2 = 0.0879$	$R_1 = 0.0610$ $wR_2 = 0.0835$	$R_1 = 0.0668$ $wR_2 = 0.1026$
CCDC No.	2177071	2177073	2177072	2177074

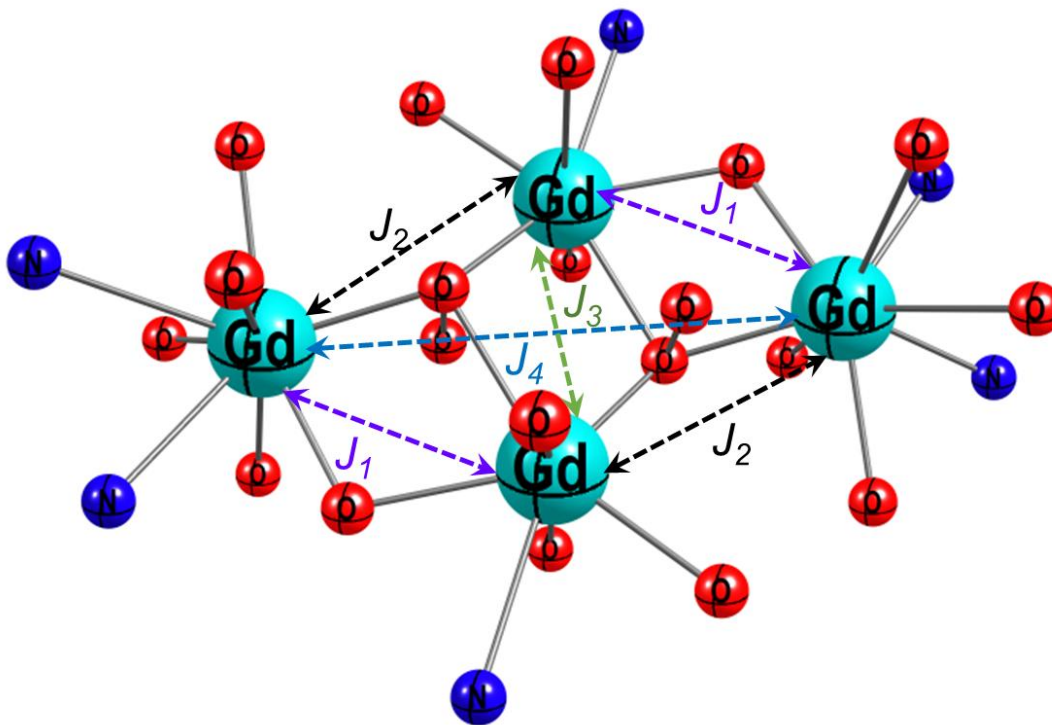
Magnetic Measurements

The direct current (dc) magnetic susceptibility measurements were performed on solid polycrystalline samples using a Quantum Design MPMS-XL SQUID magnetometer between 2 and 300 K in the applied magnetic field of 0.02 T for temperatures of 2-20 K, 0.2 T for temperatures of 20-80 K and 1 T for temperatures of 80-300 K. The sample was immobilized in a pellet made with Teflon tape. The alternative current (ac) magnetic susceptibility measurements were performed using a Quantum Design MPMS-XL SQUID magnetometer for frequencies between 1 and 1000 Hz under an oscillating field of 3 Oe and Quantum Design PPMS magnetometers for frequencies between 10 and 10000 Hz under an oscillating field of 5 Oe. These measurements were all corrected for the diamagnetic contribution as calculated with Pascal's constants.

Computational Details

To reduce the computational cost all the density functional theory (DFT) and multireference calculations were performed on a truncated model of the X-ray crystal structure, where the $-\text{CH}_3$ group of the pivalic acid was replaced with the $-\text{H}$ atom. All the hydrogen atoms in the truncated model were optimized using the BP86 level of theory⁶⁰⁻⁶¹ and def2-SVP basis sets⁶²⁻⁶³ (see ESI for the optimized coordinates). All the DFT calculations were performed using the ORCA 4.2.1

code^{1,2,64-65} Scalar relativistic DFT calculations were performed on complex **1** to analyse the electronic structure and magnetic exchange between the Gd^{III} centres. The scalar relativistic effects were accounted for by Douglas-Kroll-Hess (DKH) approximation⁶⁶ as implemented in ORCA. We have employed the B3LYP level of theory⁶⁷ with all-electron SARC basis sets for Gd centres and DKH-adapted def2-TZVP(-f) basis set for the atoms N and O atoms (i.e., the atoms in the first coordination sphere), while DKH-adapted def2-SVP basis set was used for C and H atoms. The dispersion interaction is accounted for by Grimme's dispersion along with Becke-Johnson damping (D3BJ)⁶⁸⁻⁶⁹ as implemented in ORCA. To speed up the calculations, resolution-of-identity-chain-of-sphere (RIJCOSX) formalism was employed with large GRID settings i.e., "GRID9" for Gd and "GRID6" for the rest of the atoms as implemented in ORCA. The magnetic exchange coupling between the Gd^{III} centres was calculated using Noodleman's broken-symmetry (BS) formalism.⁷⁰ The BS solutions were obtained by reading the converged natural orbital of the high-spin state ($S = 14$), followed by flipping the spin on the desired Gd centres. The correctness of the BS solution was verified by analysing the spin populations at Gd^{III} centers. Here, we have computed six different BS solutions and employed a pair-wise exchange model⁷¹ to calculate the J values in complex **1** (see ESI for details). Here we have estimated four interactions J_1 (wing-body), J_2 (wing-body), J_3 (body-body), and J_4 (wing-wing), using a pair-wise exchange model. Additionally, the ORCA_ECA utility was used to compute the relative energies of all possible spin states through diagonalization of the computed spin-Hamiltonian parameters. To further understand the mechanism of magnetic exchange between the Gd^{III} centres, three different dinuclear model complexes were prepared by substituting the other two Gd^{III} ions with diamagnetic La^{III} ions. These three dinuclear complexes M_1 , M_2 , and M_3 correspond to the J_1 , J_2 , and J_3 interaction of complex **1** (see ESI for details).



Scheme 1. DFT computed magnetic exchange pathways in **1**. Only the core structure of **1** is shown in the picture for clarity.

All the multireference calculations were performed on the truncated model of **2**, **3**, and **4** using an Open MOLCAS code.⁷²⁻⁷³ The spin-Hamiltonian parameters were calculated using a complete active space self-consistent field (CASSCF) method.⁷⁴ Here, we have employed the ANO-RCC-VDZP type basis set for the paramagnetic ions (Dy^{III} , Er^{III} , and Tb^{III}) while the ANO-RCC-VDZ type basis set was used for the rest of the atoms.⁷⁵⁻⁷⁶ The details of the basis set and contraction scheme are provided in the ESI. To speed up the calculations, the two-electron integrals were computed using the resolution of identity Cholesky decomposition (RICD) approximation. The single-ion properties of Tb^{III} , Dy^{III} , and Er^{III} in complexes **2-4** were calculated by replacing other paramagnetic ions in the cluster with their diamagnetic Lu^{III} analogue. For CASSCF calculations, the active space comprises CAS($n,7$), where n represents the number of active electrons in seven

active 4*f*-orbitals ($n = 8, 9,$ and 11 for $\text{Tb}^{\text{III}}, \text{Dy}^{\text{III}},$ and Er^{III} , respectively). Using these active spaces, we have computed 7 septets, 94 quintets, and 112 triplets for Tb^{III} ions, 21 sextets for Dy^{III} ions, 35 quartets, and 112 doublets for Er^{III} ions in **2-4**. Subsequently, these states were mixed in the spin-orbit restricted active space state interaction (SO-RASSI) module to compute the spin-orbit states.⁷⁷ The calculated spin-free energies and SOC states for **2-4** are reported in Tables S17-S28. The computed spin-orbit coupled (SOC) states were used to calculate the *g*-values, crystal field parameters, transition magnetic moments, magnetic susceptibility, and magnetization of individual $\text{Tb}^{\text{III}}, \text{Dy}^{\text{III}},$ and Er^{III} ions with the SINGLE_ANISO module⁷⁸ as implemented in MOLCAS. The obtained *g*-tensors and their orientations and the energies of computed SOC states of individual single-ion were combined to simulate the magnetic properties and exchange spectrum (dipolar and exchange contributions) of the tetranuclear complexes **2-4** using POLY_ANISO code.⁷⁹⁻⁸¹

Synthesis

The ligand LH₄ was prepared by following a reported procedure.⁵⁰

General Synthetic Procedure for the Preparation of the Complexes 1-4

LH₄ (0.040 g, 0.11 mmol) and LnCl₃·6H₂O (0.22 mmol) were taken together in methanol (25 mL) immediately giving a clear, yellow-coloured solution which was allowed to stir for 15 minutes at room temperature. Then, triethylamine (0.55 mmol) was added dropwise to the reaction mixture and subsequently, hydrogen peroxide (34.5-36.5%) (0.11 mmol) was added followed by the addition of pivalic acid (0.22 mmol). The reaction mixture was stirred overnight at room temperature, filtered and the solvent removed in vacuo affording a yellow solid residue which was dissolved in methanol to which a few drops of chloroform were added. This solution

was kept undisturbed at room temperature. Suitable crystals for X-ray diffraction were obtained by slow evaporation of the solvents within 3-4 days. Specific details of each reaction and the characterization data of the complexes are given below.

[Gd₄(LH₂)₂(η^1 -Piv)₂(η^2 -Piv)₂(μ_3 -O₂)₂(H₂O)₂] \cdot 2MeOH (1)

Quantities: LH₄ (0.040g, 0.11 mmol), GdCl₃ \cdot 6H₂O (0.083g, 0.22 mmol), H₂O₂ (0.11 mmol), Pivalic acid (0.22 mmol), Et₃N (0.55 mmol). Yield: 0.036 g, 70.05% (based on the Gd^{III} salt). IR (KBr) cm⁻¹: 3330 (br), 2958 (br), 2914 (br), 2866 (br), 1612(s), 1566 (s), 1540 (s), 1477 (s), 1431 (s), 1355 (s), 1194 (s), 1068 (s), 848 (s), 754 (s). Anal. Calcd. For C₅₈H₈₈Gd₄N₈O₂₄ (1912.28): C, 36.47; H, 4.59; N, 5.81 Found: C, 36.02; H, 4.17; N, 5.55

[Tb₄(LH₂)₂(η^1 -Piv)₂(η^2 -Piv)₂(μ_3 -O₂)₂(H₂O)₂] \cdot 2MeOH (2)

Quantities: LH₄ (0.040 g, 0.11 mmol), TbCl₃ \cdot 6H₂O (0.041g, 0.11 mmol), Pivalic acid (0.22 mmol), H₂O₂ (0.11 mmol), Et₃N (0.55 mmol). Yield: 0.039 g, 76.02% (based on the Tb^{III} salt). Mp: >250 °C (d). IR (KBr) cm⁻¹: 3332 (br), 2969 (br), 2912 (br), 2866 (s), 1612 (s), 1540 (w), 1446 (s), 1431 (w), 1371 (s), 1274 (w), 1224 (w), 1195 (s), 1068 (s), 1016 (s), 900 (w), 849 (s), 754 (s), 691 (w). Anal. Calcd. For C₅₈ H₈₈ Tb₄ N₈ O₂₄ (1916.29): C, 36.34; H, 4.63; N, 5.85 Found: C, 36.01; H, 4.24; N, 5.64.

[Dy₄(LH₂)₂(η^1 -Piv)₂(η^2 -Piv)₂(μ_3 -O₂)₂(H₂O)₂] \cdot 2MeOH (3)

Quantities: LH₄ (0.040 g, 0.11 mmol), DyCl₃ \cdot 6H₂O (0.082 g, 0.22 mmol), H₂O₂ (0.11 mmol), pivalic acid (0.22 mmol), Et₃N (0.55 mmol). Yield: 0.041 g, 80.04% (based on the Dy^{III} salt). Mp: >200 °C (d). IR (KBr) cm⁻¹: 3337 (br), 2961 (br), 2867 (br), 1614 (S), 1541 (w), 1479 (s), 1431 (w), 1356 (s), 1275 (w), 1225 (s), 1197 (s), 1152 (s), 1070 (s), 1017 (s), 901 (s), 850 (s), 755

(s), 709 (w), 692 (s). Anal. Calcd. For C₅₈ H₈₈ Dy₄ N₈ O₂₄ (1936.30): C, 36.07; H, 4.59; N, 5.80 Found: C, 35.85; H, 4.45; N, 5.67.

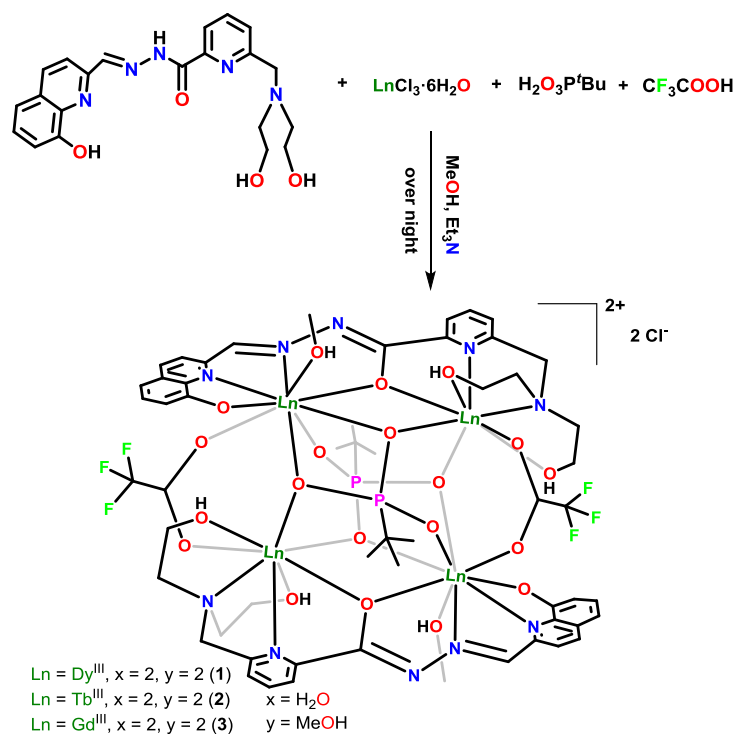
[Er₄(LH₂)₂(η^1 -Piv)₂(η^2 -Piv)₂(μ_3 -O₂)₂(H₂O)₂] \cdot 2MeOH (4)

Quantities: LH₄ (0.040g, 0.11 mmol), ErCl₃ \cdot 6H₂O (0.0849g, 0.22 mmol), pivalic acid (0.22 mmol), H₂O₂ (0.11 mmol), Et₃N (0.55 mmol). Yield: 0.037 g, 72.4% (based on the Er^{III} salt). Mp: >250 °C (d). IR (KBr) cm⁻¹: 3347 (br), 2966 (br), 2866 (w), 1616 (s), 1546 (s), 1479 (s), 1355 (s), 1275 (w), 1225 (w), 1198 (s), 1152 (s), 1071 (s), 901 (s), 852 (s), 755 (s), 692 (s), 644 (w). Anal. Calcd. For C₅₈ H₈₈ Er₄ N₈ O₂₄ (1944.31): C, 35.66; H, 4.27; N, 5.94 Found: C, 35.30; H, 4.11; N, 5.71

Results and Discussion

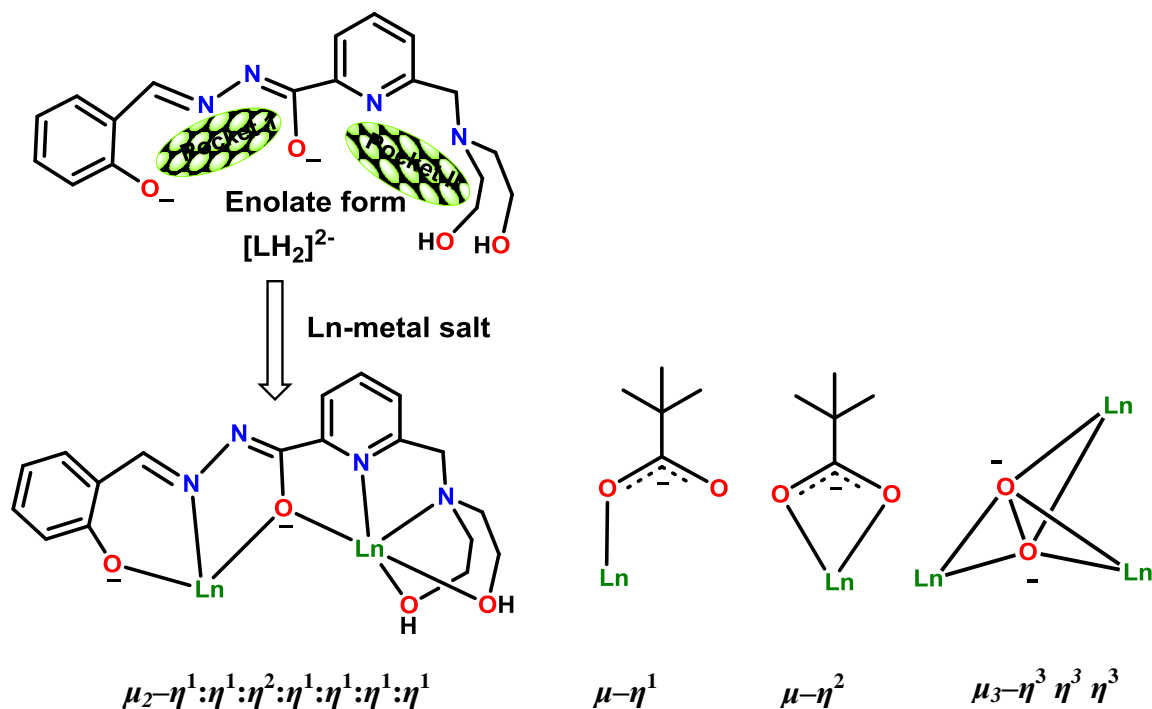
Synthetic Aspects

Among polyfunctional ligands, aroylhydrazone-based Schiff base ligands have found a great utility to construct multi-nuclear lanthanide ensembles of various nuclearities, geometries, and topologies.^{44-49, 82-86} The versatility of this ligand family arises from several features including their flexibility involving C-C and C-N bond rotation and capability of coordinating to the metal centre in keto/enolate forms, depending on the reaction conditions. We have been involved in the use of this ligand system for some time now with considerable success (Scheme 2). The tetranuclear assembly shown in Scheme 2 contains two dinuclear subunits connected to each other by the phosphonate ligand.



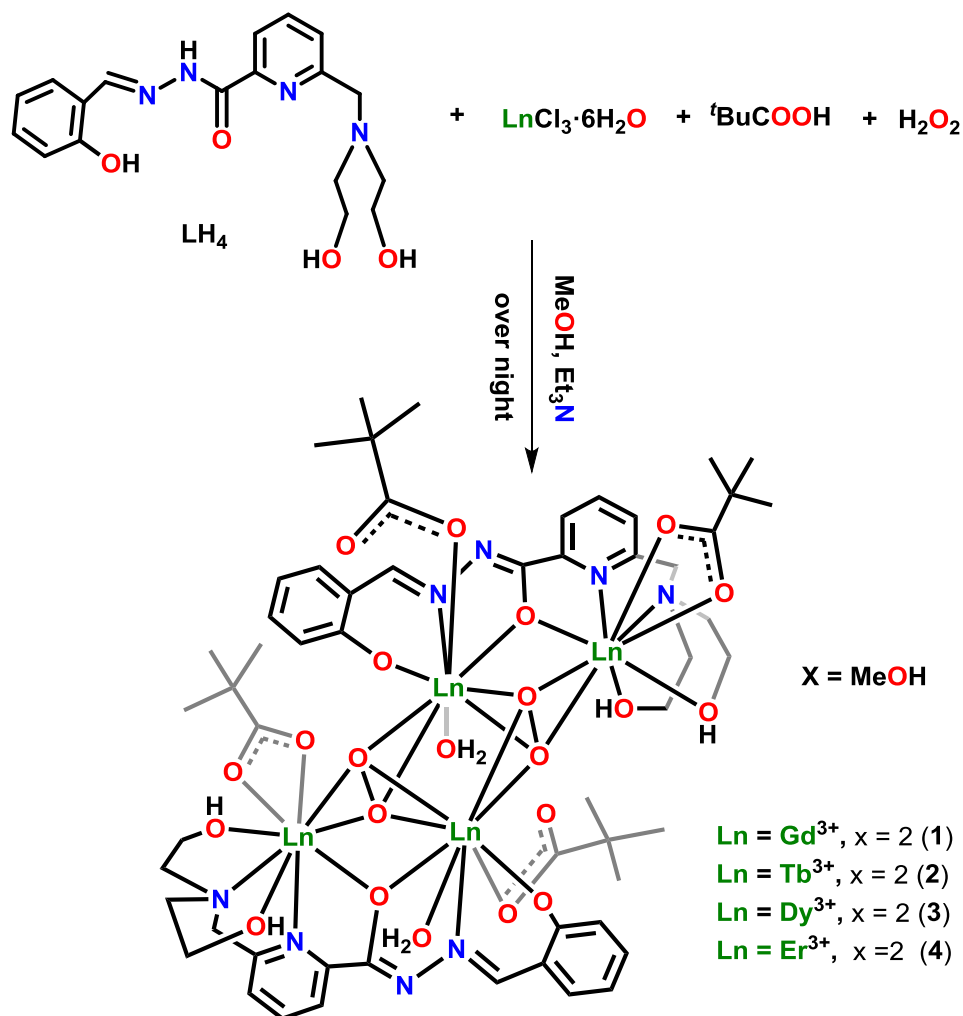
Scheme 2. Synthesis of a phosphonate assisted tetranuclear complex, $[\text{Ln}_4(\text{LH}_2)_2(\text{O}_3\text{P}'\text{Bu})_2(\mu_2\text{-}\eta^1\eta^1\text{tfa})_2][2\text{Cl}]$ ($\text{Ln} = \text{Dy}^{\text{III}}$ (1), Tb^{III} (2) and Gd^{III} (3)).⁴⁹

Inspired by the above results, we were interested in examining the coordination response of the peroxide ligand in conjunction with LH_4 . Specifically, we were interested to examine if the peroxide ligand formed under the reaction conditions binds in a side-on or end-on manner (Scheme S1) and if the peroxide ligand can also assist in bridging metal complex sub-units similar to what has been shown by us and others for phosphonate ligands.^{49, 87} The ligand LH_4 contains two unsymmetrical pockets with seven coordination sites which can be partitioned as follows: a tridentate pocket, consisting of a phenolic oxygen, an imine N, and an enolate O (2O,1N) while the other is pentadentate pocket, consisting of a pyridine N, a common enolate oxygen and a diethanolamine motif (2N, 3O) (Scheme 3). We anticipated that the ligand $[\text{LH}_2]^{2-}$ can accommodate two lanthanide ions in its pockets (Scheme 3), affording a dinuclear motif which can be bridged by peroxide ions to afford a tetranuclear complex (Scheme 3).



Scheme 3. The unsymmetrical coordination pockets of LH₄ and various coordination modes of deprotonated LH₄ and coligands.

In addition to using the ligands LH₄ and H₂O₂ we have also used pivalic acid as a co-ligand to fill the remaining sites on metal centres. Accordingly, the reaction of LH₄, LnCl₃·6H₂O, hydrogen peroxide, and pivalic acid in the presence of the base triethylamine in a molar ratio of 1:1:1:2:5 afforded tetranuclear complexes [Ln₄(LH₂)₂(η¹-Piv)₂(η²-Piv)₂(μ₃-O₂)₂(H₂O)₂]·2MeOH, where Ln = Gd^{III} (**1**), Tb^{III} (**2**), Dy^{III} (**3**), Er^{III} (**4**) (Scheme 4).



Scheme 4. Synthesis of Ln₄ complexes **1-4**.

To check the phase purity of the complexes **1-4**, powder X-ray data were collected. The experimental and simulated PXRD pattern of **1-4** were found to match quite well indicating the phase purity of the complexes (Figures S1-S4).

To assess the thermal stability of **1-4**, thermogravimetric analysis (TGA) was carried out in the temperature range of 25–600 °C. As shown in Figures S5-8, **1-4** reveal a weight loss of approximately 8-9% from 25 °C to 230 °C, which corresponds to the loss of two methanol molecules, two coordinated water molecules, and two peroxo ions (calcd: 8-9%). After the

temperature range of 550 °C, a continuous weight loss is observed for all the complexes indicating the decomposition of the complexes (Figures S5-S8).

X-ray Crystallography

Suitable crystals for single-crystal X-ray diffraction study were obtained by slow evaporation of the methanol/chloroform (4:1) solutions of **1-4**, within 3-4 days. A single-crystal X-ray diffraction study reveals that **1-4** are charge-neutral, isostructural, and crystallize in a triclinic system in the space group $P-1$ with $Z = 1$. In view of the structural similarity of the complexes, we are providing a description of these using **1** as a representative example. A perspective view of **1** is given in Figure 1 and those of complexes **2-4** are given in the Electronic Supporting Information (ESI) (Figures S9-S11). Selected bond lengths and bond angles of **1** are given in Table 2 while those of complexes **2-4** are given in ESI (Tables S1-S3.).

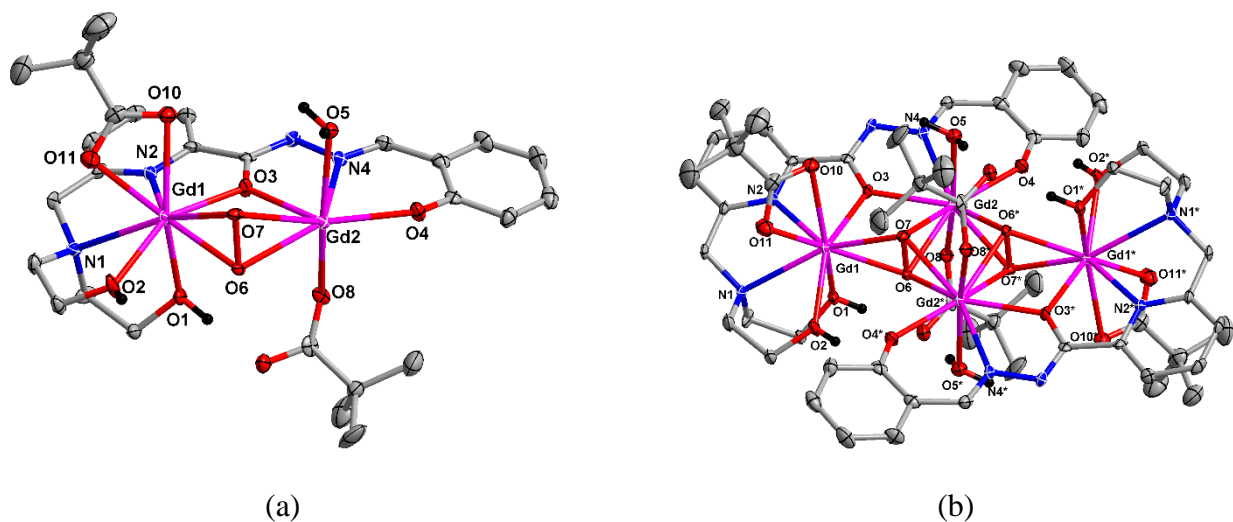


Figure 1. (a) Asymmetric unit and (b) Molecular structure of **1**. Thermal ellipsoids at a 50% probability level are shown (selected hydrogen atoms and the solvent molecules have been omitted for clarity). Color codes: N = blue; O = red; C = grey; Gd= pink and H = black)

Table 2. Selected bond angles (°) and bond distances (Å) of **1**

Bond distances around Gd1		Bond distances around Gd2		O-O bond distance	
Gd(1)-O(1)	2.426(3)	Gd(2)-O(3)	2.357(3)	O(6)-O(7)	1.530(4)
Gd(1)-O(2)	2.386(3)	Gd(2)-O(4)	2.331(3)	Bond angles around Gd atoms	
Gd(1)-O(3)	2.314(3)	Gd(2)-O(5)	2.445(3)		
Gd(1)-O(6)	2.308(3)	Gd(2)-O(6)	2.439(3)	O(6)-Gd(2)-O(7)	35.15(9)
Gd(1)-O(7)	2.332(3)	Gd(2)-O(7)	2.602(3)	O(6)*-Gd(2)-O(7)*	37.78(10)
Gd(1)-O(10)	2.515(3)	Gd(2)-O(6)*	2.337(3)	O(7)-Gd(1)-O(6)	38.50(10)
Gd(1)-O(11)	2.447(3)	Gd(2)-O(7)*	2.385(3)	Gd(2)-O(6)-Gd(1)	105.56(11)
Gd(1)-N(1)	2.657(4)	Gd(2)-O(8)	2.332(3)	Gd(2)-O(7)-Gd(1)	99.88(10)
Gd(1)-N(2)	2.501(4)	Gd(2)-N(4)	2.641(4)	Gd(2)-O(6)-Gd(2)*	101.15(11)
				Gd(2)-O(7)-Gd(2)*	95.33(10)
				Gd(2)-O(3)-Gd(1)	108.05(12)

The asymmetric unit comprises of a doubly deprotonated ligand $[\text{LH}_2]^{2-}$ which accommodates two Gd^{III} ions in its two multidentate flexible pockets [tridentate (ONO) and pentadentate (ONNOO) (scorpionate type)]. The metal centres in the asymmetric unit are also bridged by the peroxide ion. The latter binds in a $\mu_3\text{-}\eta^2\text{:}\eta^2\text{:}\eta^2$ fashion to another sub-unit affording the tetranuclear core, $[\text{Gd}_4(\text{LH}_2)_2(\text{O}_2)_2]^{4+}$ (Figure 2). The remaining sites on the metal centres in the tetranuclear assembly are filled by four pivalate ions and two water molecules. Interestingly, the pivalate ions function as terminal ligands. Thus, **1** consists of four Gd^{III} ions, two di anionic ligands, $[\text{LH}_2]^{2-}$, two peroxide anions, four pivalate anions, and two water molecules. The coordination pattern of each of these ligands is shown in Scheme 3. The peroxide ligand functions in a side-on binding and generates a Gd_4O_6 core by bridging two dinuclear subunits (Figure 2b). This results in three Gd_2O_2 four-membered rings supported by a single peroxide ligand, in a butter-fly type topology (Figure 2c). The four Gd centres lie in the same plane with two types of Gd---Gd distances, $\text{Gd2-Gd1} = 3.780 \text{ \AA}$ and $\text{Gd2-Gd1}^* = 4.1983 \text{ \AA}$.

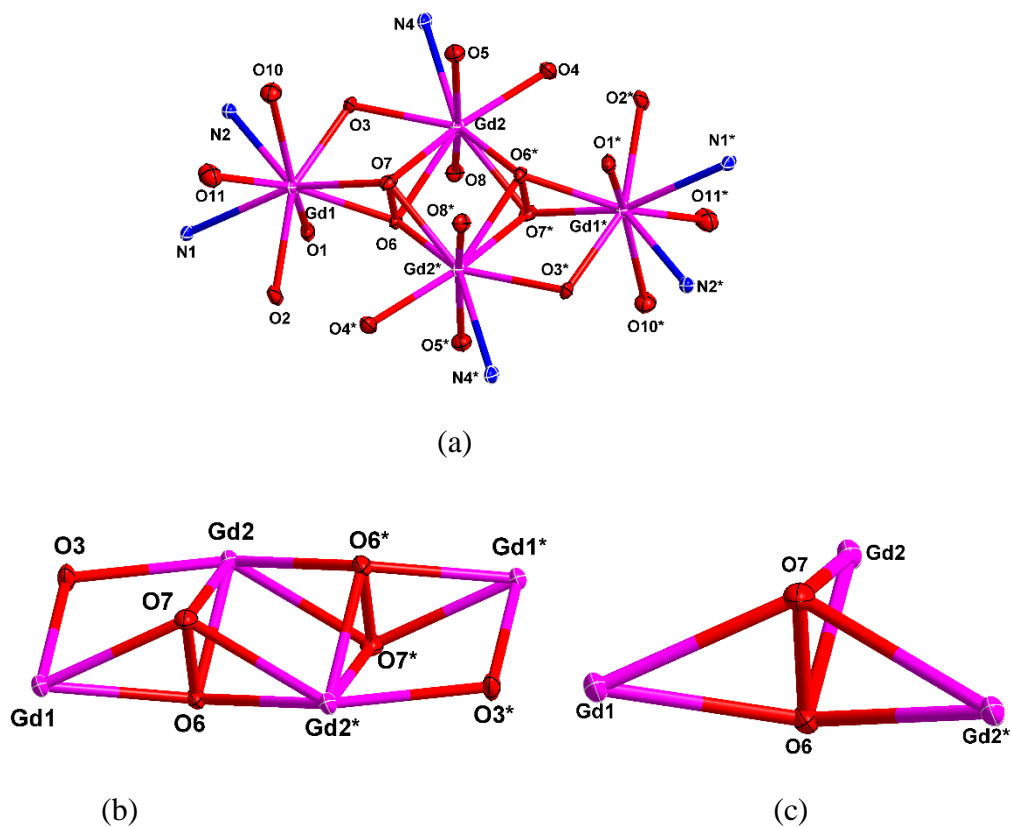


Figure 2. a) Core structure of **1** b) Gd_4O_6 core of **1** c) butterfly topology around peroxide ion. For clarity, the outer backbone of ligands and co-ligands are omitted.

Based on the immediate coordination geometry two types of Gd^{III} can be identified. Thus, Gd1 has an N_3O_6 environment in a spherical capped square antiprism while Gd2 has an N_2O_7 coordination environment in a muffin geometry. The geometry around the Gd^{III} centres was determined by the SHAPE program⁸⁸⁻⁸⁹ (Figure 3, Table S4).

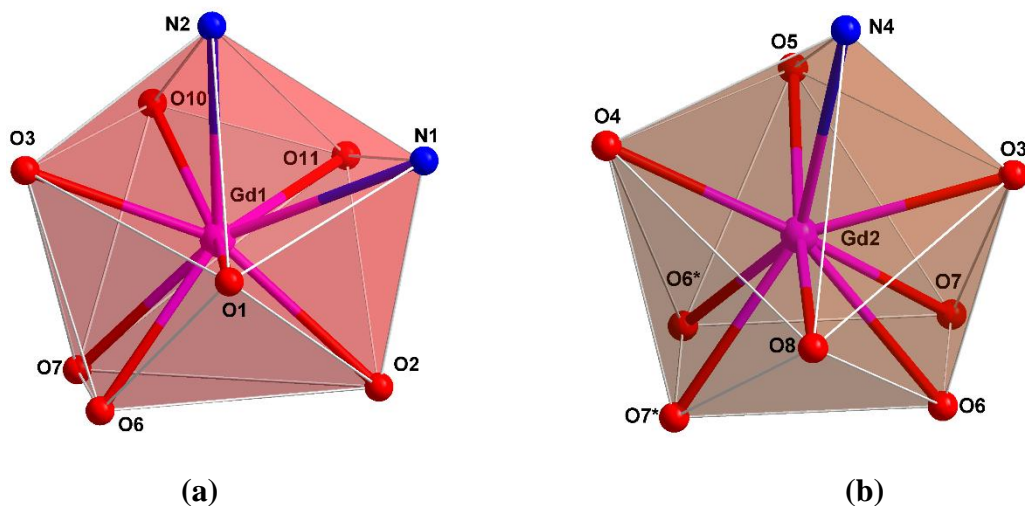


Figure 3. (a) Spherical capped square antiprism coordination geometry around Gd1 and (b) Muffin geometry around Gd2.

The Gd–O and Gd–N bond lengths fall in a range of 2.308–2.602 Å and 2.501–2.651 Å respectively. The peroxide (O–O) bond length is found to be 2.530 Å which is consistent with what was found previously in analogous lanthanide complexes (ESI, Table S5).⁹⁰⁻⁹⁶

The crystal structure of **1** reveals that several types of intra/inter molecular hydrogen bonding are present leading to a 2D supramolecular architecture (Figures S12-13, Tables S6-S7).

Although peroxide binding in lanthanide complexes is quite sparse, there are a few examples which are listed in Table S5 in the ESI. Among these only example, that too a heterometallic complex, $\{[\text{Dy}_3\text{Ni}_3(\text{H}_2\text{O})_3(\text{mpko})_9(\text{O}_2)(\text{NO}_3)_3](\text{ClO}_4)\cdot 3\text{CH}_3\text{OH}\cdot 3\text{CH}_3\text{CN}\}$ is a zero-field SMM (Table S5, ESI).⁹⁴ And, similarly there are only two heterometallic complexes, containing peroxide coordination, where MCE properties are reported (Table S5, ESI).⁹³ In light of this the results presented herein add much value to the existing literature.

Magnetic Studies

The temperature dependence of the molar magnetic susceptibilities (χ_M) of the tetranuclear complexes (Figure 4) were measured from 2 to 300 K temperature. The observed room

temperature $\chi_M T$ values of 31.75, 42.23, 53.2 and 42.73 cm³ K mol⁻¹ for complexes **1-4** respectively are found to be in reasonably good agreement with the expected values for four isolated Ln^{III} ions; 31.48 cm³ K mol⁻¹ for Gd^{III} (⁸S_{7/2} $g_J = 2$), 47.28 cm³ K mol⁻¹ for Tb^{III} (⁷F₆ and $g_J = 3/2$), 56.68 cm³ K mol⁻¹ for Dy^{III} (⁶H_{15/2} and $g_J = 4/3$), and 45.92 cm³ K mol⁻¹ for Er^{III} (⁴I_{15/2} and $g_J = 6/5$).⁹⁷ Upon lowering the temperature the $\chi_M T$ values of **1** remain constant down to 30 K and then decrease until 2 K reaching the minimum values of 19.59 cm³ K mol⁻¹ respectively. The magnetic behaviour of **1** is a clear indication of antiferromagnetic exchange interactions at low temperatures. For the isotropic Gd^{III} based system, the antiferromagnetic behaviour in the magnetic susceptibility can be described by employing the exchange interactions between the different metal centres ($H = -\sum_{i,j} J(\vec{S}_i \cdot \vec{S}_j)$). The four Gd^{III} ions forming the structure are represented in Figure S14, with their respective oxygen-bridges and the four different exchange interactions described as: J_1 between Gd2...Gd1 via O3/O6/O7 (average angle value of 104.5°), J_2 between Gd2...Gd1* via O6*/O7* (average angle value of 127.6°), J_3 between Gd2...Gd2* via O7/O6 (average angle value of 98.1°) and J_4 between Gd1...Gd1* via O6/O7-Gd2/Gd2*-O6*/O7*. The best-fitted parameters (Figure S15) are extracted using a homemade program assuming that J_4 is negligible in comparison to the other contributions. The following parameters have been determined: $g = 2.017$, $J_1 = -0.0690$, $J_2 = -0.0349$ and $J_3 = -0.0938$ cm⁻¹. The negative value of the different J s indicates the antiferromagnetic interactions between the different Gd^{III} centres. It is well known that the magnetic exchange interaction intensity is dependent on the Gd-O-Gd angle.⁹⁸ Indeed, the acute and obtuse angle values lead to the strongest (J_1 and J_3) and weakest (J_2) antiferromagnetic exchange interaction constants, respectively.

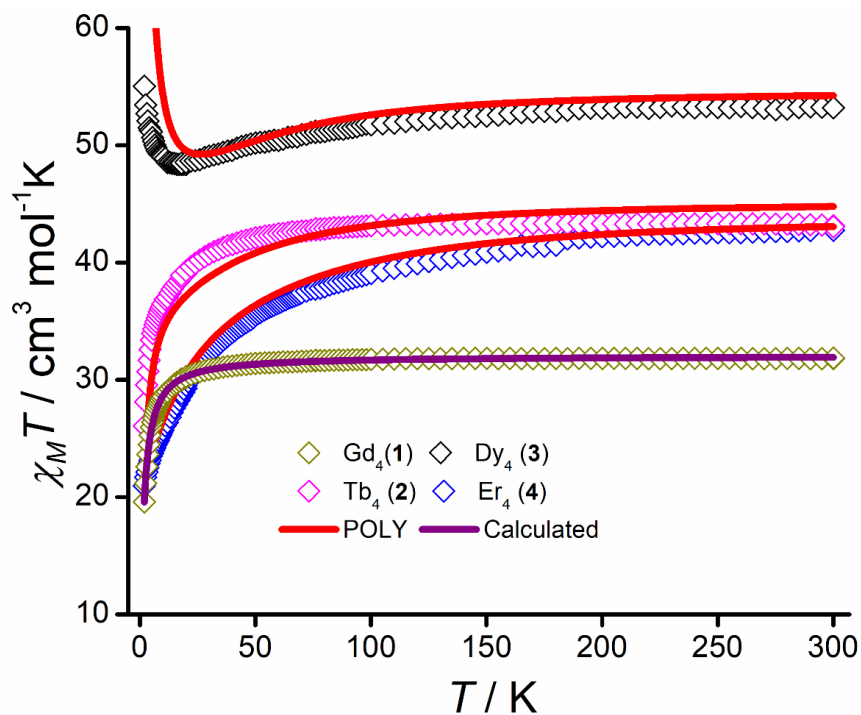


Figure 4. Thermal dependence of the molar magnetic susceptibility for **1** (green), **2** (magenta), **3** (black), and **4** (blue) from 2 to 300 K. Purple solid line represent the best curve fit of the $\chi_M T$ product of **1**. The solid red solid lines represent the POLY_ANISO simulated data. Note: we have reduced the simulated data by 4% to meet the experimental values.

The $\chi_M T$ values of **2** remain constant down to 50 K and then decrease until 2 K reaching the minimum value of $26.07 \text{ cm}^3 \text{ K mol}^{-1}$. The $\chi_M T$ product **3** decreases from 300 K to 17 K ($48.35 \text{ cm}^3 \text{ K mol}^{-1}$) and then increases at lower temperature reaching the maximum value of $55.02 \text{ cm}^3 \text{ K mol}^{-1}$ at 2 K while the $\chi_M T$ product for **4** decreases continuously from room temperature to 2 K ($20.96 \text{ cm}^3 \text{ K mol}^{-1}$). The decrease of $\chi_M T$ products for **2**, **3**, and **4** could be attributed to the combination of both crystal-field effects and antiferromagnetic interactions. For **3**, additional significant ferromagnetic dipolar interactions are observed in the low-temperature range.

For **1**, the field dependence of the magnetization increases with increasing applied magnetic field, reaching a saturation value of $28.2 N\beta$ at 5T, which agrees with the theoretical value for the four isotropic Gd^{III} ions. The magnetization data for **1** was simulated with the Brillouin formula for $g = 2.017$ and $S = 7/2$ (Figure S15, red line). As displayed in Figure S15, the differences existent between the experimental data and the simulation, support the antiferromagnetic interactions previously determined in the system **1**. Magnetization shows a classical behaviour with values of $18.3 N\beta$, $19.3 N\beta$ and $17 N\beta$ at 50 kOe for the three Tb^{III} , Dy^{III} and Er^{III} ions in their respective complexes, presenting the associated magnetic anisotropy (Figure S15).

Magnetothermal Property of 1

The weak magnetic couplings usually featured in Gd-systems, together with the high metal/ligand mass ratio, are some characteristics that make this system an interesting candidate for the *Magnetocaloric Effect* (MCE). To evaluate the MCE, the magnetization data for **1** was measured between 2 and 15 K up to a maximum magnetic field of 13 T (Figure 5A). Subsequently, the change in the magnetic entropy ($-\Delta S_m$) of the system was calculated by applying the Maxwell equations ($\Delta S_m(T) = \int (\partial M / \partial T) dH$)^{22, 99} to the magnetic data mentioned above. The dependence of the $-\Delta S_m$ with the temperature is represented in Figure 5B, corresponding to a gradual growth with the decreasing temperature and increasing field. The maximum $-\Delta S_m$ experimentally observed corresponds to $33.60 J K^{-1} Kg^{-1}$ at 4 K and $\Delta H = 13 T$; which is close to the theoretical limiting value of $36.45 J K^{-1} Kg^{-1}$ calculated from the expression $\Delta S = nR \ln(2S + 1) / M_W$ (where R is the gas constant, n the number of non-interacting spins (4), $S = 7/2$, and $M_W = 1897 g/mol$). In general, the deviation between maximum calculated and experimental values of $-\Delta S_m$ is due to the antiferromagnetic interactions between the metal

centres as reported previously¹⁰⁰⁻¹⁰⁵. In fact, even larger discrepancy between calculated and experimental values is found in some Gd₄ clusters^{101, 103} which has been attributed to strong antiferromagnetic coupling.

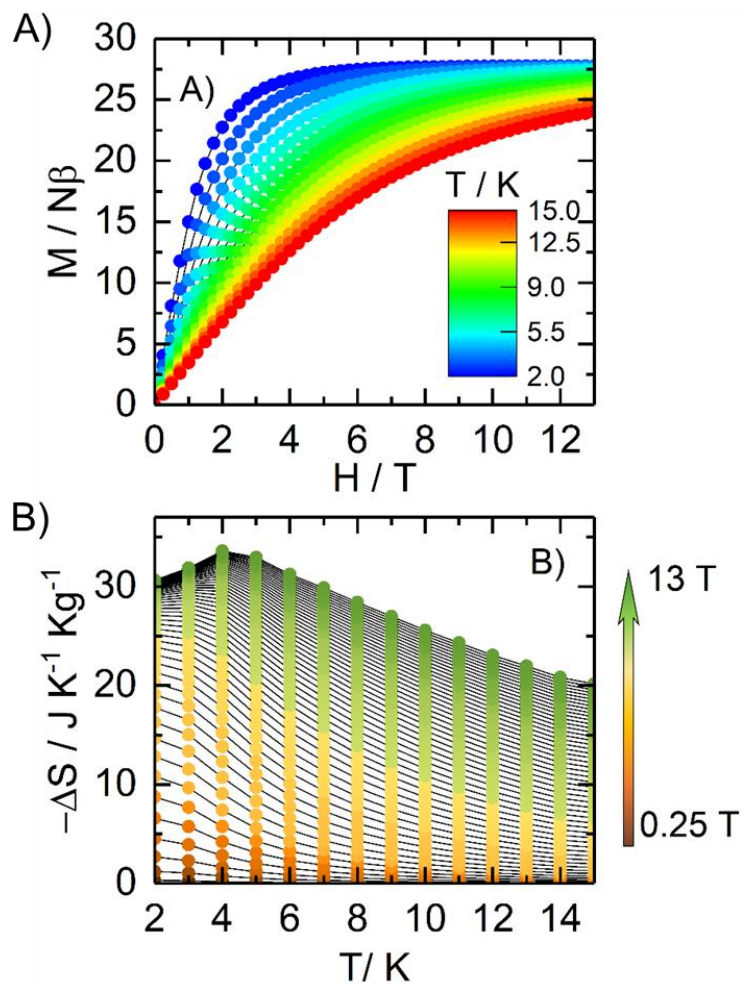


Figure 5. A) Field dependence of the magnetization from 2 to 15 K for **1**. B) Temperature dependence of $-\Delta S_m$ obtained from the magnetization corresponding to selected ΔH for **1**.

The MCE properties of known molecular Gd₄ clusters are summarized in Table 3. Interestingly, **1** reveals a significant MCE value (Table 3).

1 has a slightly lower value of $-\Delta S_m$ (maximum) in comparison to three-dimensional systems such as GdF_3 ,³⁷ $Gd(OH)CO_3$ ³⁶ and others¹²¹⁻¹²².

In principle, it may be possible to achieve larger MCE values in peroxide linked clusters if the system can be designed to have large metal/ligand ratio or less diamagnetic contents with suitable exchange coupling.

Table 3. The MCE data for **1** along with those for representative examples of Gd_4 clusters

S. No.	Compound	$-\Delta S_m$ ($J K^{-1} Kg^{-1}$) (ΔH)	Temp. (K)	Ref.
1.	$[Gd_4(SO_4)_4(\mu_3-OH)_4(H_2O)_4]$	51.29 (7T)	2	106
2.	$[Gd_4(OAc)_4(acac)_8(H_2O)_4]$	37.7 (7T)	2.4	31
3.	$[Gd_4(HL)_4(\mu_2-CH_3O)_4] \cdot 4CH_3OH$; $H_3L = N'-(2-hydroxybenzylidene)-6-(hydroxymethyl)picolinohydrazide$	34.46 (7T)	2	107
4.	$[Gd_4(CO_3)(L)_4(acac)_2(H_2O)_4] \cdot 2CH_3CN$; $H_2L = 2-(hydroxyimino)-2-[(3-methoxyl-2-hydroxyphenyl)methylene]hydrazide$	31.23(7T)	2	108
5.	$[Gd_4(HL)_4(\mu_2-CH_3O)_4] \cdot 4CH_3OH$; $H_2L = N'-(4-diethylamino-2-hydroxybenzylidene)-6-(hydroxymethyl)picolinohydrazide$	29.2(7T)	2	109
6.	$[Gd_4(acac)_6(L)_2(CH_3O)_2(CH_3OH)_4]$; $H_2L = N-((2,3-dioxidophenyl)methylidene)pyridine-2-carbohydrazonate$	27.96(7T)	2	110
7.	$[Gd_4(CO_3)(L)_4(acac)_2(MeOH)_2(H_2O)_2] \cdot MeOH \cdot H_2O$; $H_2L = 2-(hydroxyimino)-2-[(3-methoxyl-2-hydroxyphenyl)methylene]hydrazide$	27.06(7T)	2.5	108
8.	$[Gd_4(\mu_3-OH)_4(L)_4(\mu_2-piv)_4(MeOH)_4]$; $LH = [1,3-bis(o-methoxyphenyl)-propane-1,3-dione]$	25.57(7T)	3	111
9.	$[Gd_4(acac)_4(L)_6(\mu_3-OH)_2] \cdot CH_3CN \cdot 0.5CH_2Cl_2$; $HL = 5-(benzylidene)amino-8-hydroxyquinoline$	25.08(7T)	2	112
10.	$[Gd_4L_4(OH)_2]-(OAc)_2 \cdot 4H_2O$	24.4(7T)	3	113
11.	$[Gd_4(acac)_4(\mu_3-OH)_2(L)_6] \cdot 4CH_3CN$; $HL = 5-(4-ethylbenzylidene)-8-hydroxyquinoline$	23.37(7T)	2	114

12. $\text{Gd}_4(\text{L})_4(\text{CO}_3)(\text{acac})_2(\text{CH}_3\text{OH})_4 \cdot 2\text{CH}_3\text{OH} \cdot \text{CH}_2\text{Cl}_2$; $\text{H}_2\text{L} = 2\text{-}(\text{hydroxyimino})\text{-}2\text{-}[(5\text{-methyl-}2\text{-hydroxyphenyl)methylene]hydrazide}$	21.43(7T)	5	101
13. $\{[\text{Gd}_4(\text{L})_6(\text{pbd})_4(\mu_3\text{-OH})_2] \cdot 2\text{CH}_3\text{CN}\}$; HL = 5-(benzylideneamino)quinolin-8-ol	21.41(7T)	2	115
14. $[\text{Gd}_4(\text{N}_3)_4(\text{Tpz})_8]$; Tpz = tris(pyrazolyl)borate)	20.9(7T)	3	116
15. $\text{Gd}_4(\text{L})_2(\text{dbm})_6(\text{C}_2\text{H}_5\text{OH})_2$; $\text{H}_3\text{L} = (6\text{-hydroxymethyl})\text{-N}'\text{-}((2,3\text{-dihydroxyphenyl})\text{-methylene})\text{picolinohydrazide}$	20.26(7T)	2	117
16. $[\text{Gd}_4(\mu_3\text{-OH})_2(\text{L})_6(\text{acac})_4] \cdot 2\text{CH}_3\text{CN}$; HL = 5-(4-o-hydroxybenzylidene)-8-hydroxylquinoline	18.85(7T)	2.5	118
17. $[\text{Gd}_4(\mu_3\text{-OH})_2(\text{tmhd})_4(\text{L})_6] \cdot 2\text{CH}_3\text{CN}$; HL = 5-phenyl-8-hydroxylquinoline	17.94(7T)	2	119
18. $[\text{Gd}_4(\text{dbm})_4(\text{L})_6(\mu_3\text{-OH})_2] \cdot 5\text{CH}_3\text{CN} \cdot 0.5\text{CH}_2\text{Cl}_2$; HL = 5-(((3-methyl-2-thienyl)methylene)amino)-8-hydroxyquinoline	17.77(7T)	2	102
19. $\text{Gd}_4(\mu_3\text{-OH})_2(\text{L})_6(\text{tmhd})_4 \cdot \text{CH}_3\text{CN} \cdot \text{CH}_3\text{CH}_2\text{OH}$; HL = 5-(4-methoxybenzylidene)-8-hydroxylquinoline	16.21(7T)	3	120
20. Complex 1	33.40(13T)	4	This work

Dynamic Magnetic Behaviour of 2-4

To determine the existence of slow relaxation of the magnetization, dynamic magnetic susceptibility measurements were performed for the anisotropic complexes **2**, **3**, and **4**. The zero-field ac susceptibility shows for **2** and **3** an out-of-phase component, passing through maxima centred at 10 and 7 kHz, respectively (Figures S16-S17). However, for complex **4**, only the beginning of the peak is observed at the highest frequency values (Figure S18). By applying a DC magnetic field, the slow relaxation of the magnetization is enhanced, and the out-of-phase component shifts to lower frequencies because of the cancelling of the fast relaxation of the magnetization through Quantum Tunnelling of the Magnetization (QTM).¹²³ As a result, for the three compounds a double peak contribution appears whereas the relaxing fraction increases.

However, this relaxing part is not sufficient in **2** (ESI, Figure S16) and no further experiments were performed. For complexes **3** and **4**, a respective optimal magnetic field of 1 and 4 kOe (ESI, Figure S17-S19, Table S8) were determined, considering a compromise between the slowest relaxation and the intensity of the relaxing fraction. The thermal dependence of the ac magnetic susceptibility has been studied (Figures 6 and S20-S21). The relaxation time (τ) has been extracted with a modified extended Debye model for two peaks for **3** (see ESI Figure S20, Table S9), whereas it has been manually extracted for **4** (Figure S21). The thermal variation of the $\log(\tau)$ for **3** is depicted in Figure 6B, in which the two different relaxation events are represented. The dependence on the temperature is described by the contribution of Orbach and Raman processes ($\tau^{-1} = \tau_0^{-1} \exp\left(-\frac{\Delta}{kT}\right) + CT^n$) for the low frequency (L.F.) contribution (black disks) and a full direct process ($\tau^{-1} = AH^4T$) for the high frequency (H.F.) contribution (orange disks). The best fitted parameters are $\Delta = 23(2)$ K, $\tau_0 = 9(2) \cdot 10^{-7}$ s, $C = 187(99)$ K⁻ⁿ s⁻¹ and $n = 1.7(7)$ for the LF contribution; and $A = 3.18(7) \cdot 10^{-8}$ Oe⁻⁴ .K⁻¹ s⁻¹ for the HF contribution. The expected n value for Kramers ions should be 9¹²⁴ but it is well known that for molecular systems, the presence of both acoustic and optical phonons could lead to lower values between 2 and 7^{124,125} and sometimes even lower.¹²⁶⁻¹²⁷

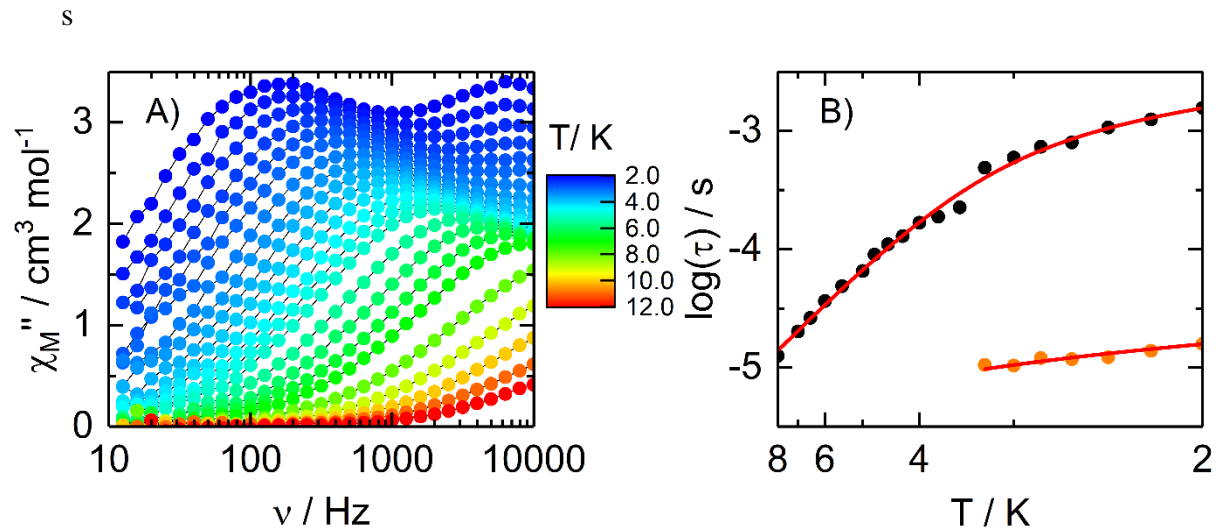


Figure 6. A) Frequency dependence of the out-of-phase susceptibility (χ_M'') of **3** at 1 kOe between 2 and 12 K. B) Thermal dependence of the relaxation times of the magnetization of **3** at 1 kOe and from 2 to 8 K. Red lines correspond to the best-fitted curve.

Concerning complex **4**, the relaxation is driven only by direct process and the details are presented in ESI with $A = 1.56(2) \cdot 10^{-13} \text{Oe}^{-4} \text{K}^{-1} \text{s}^{-1}$ (Figure S21).

Electronic Structure Calculations

Magnetic Exchange Interaction in **1**

To understand the nature of the magnetic exchange interaction in **1**, we have performed scalar relativistic broken-symmetry density functional calculations using B3LYP functional (see computational details). These broken-symmetry DFT calculations have shown a track record in computing the sign and magnitude of the magnetic exchange interaction in various polynuclear lanthanide-based complexes.¹²⁸⁻¹³⁴ In the butterfly type Ln_4 complexes, six exchange interactions connect each Gd^{III} ion, including four body-wing interactions, one body-wing, and one wing-wing interaction. In complex **1**, the Gd_4 assembly contains two dinuclear subunits connected by two peroxo ligands in the $\mu_3\text{-}\eta^3 \eta^3 \eta^3$ fashion, where each O atom of the peroxo ligand is

connected to three Gd^{III} centres. A careful inspection indicates that the four body-wing interactions in **1** can be reduced to two by symmetry arguments. Here, we have labelled the first body-wing interaction as J_1 , representing the interaction between the two Gd^{III} centres connected by one μ_2 -O bridge of pivalic acid and one peroxo bridge in the η^2 - fashion. On the other hand, the second body-wing interaction (J_2) represents the interaction between the two Gd^{III} centres connected only through one peroxo ligand in the η^2 - fashion. The body-body interaction is described as J_3 , where two peroxo ligands connect two Gd^{III} centres in the η^2 - fashion. We have also computed the wing-wing interactions (J_4) between the two Gd^{III} centres situated far apart from each other (~ 7.086 Å) and connected through multiple atoms (see Scheme 1). Using the pair-wise exchange interaction, we computed all four J (J_1 - J_4) values in **1** (see ESI for broken-symmetry energies and J values). For **1**, BS-DFT calculations predict J_1 - J_3 as antiferromagnetic interaction while J_4 as extremely weak ferromagnetic interaction. DFT calculated J values are -0.093, -0.033, -0.097 cm⁻¹ for J_1 to J_3 respectively. The computed J -values are in excellent agreement with the experimental J value of $J_1 = -0.0690$, $J_2 = -0.0349$, and $J_3 = -0.0938$ cm⁻¹, respectively. On the other hand, DFT calculated J_4 interaction is 0.001 cm⁻¹ which is extremely small compared to other J_1 - J_3 interactions due to largely separated Gd^{III} ions (~ 7.086 Å). Most importantly, DFT predicts three distinct exchange interactions with the correct trend in the magnitude as observed in the experiment. Furthermore, we have also simulated the static *DC* magnetic susceptibility and magnetization data using the DFT computed J values, and our simulated data is in excellent agreement with the experiment (see Figure S29). Spin-density analysis indicates that all the Gd^{III} centres possess a spin-density of ~ 7.014 , which results from weak spin-polarization (see Figure 7). The extent of the spin-polarization is significantly large on the connecting bridging oxygen atoms (for both the μ_2 -O bridge and η^2 -peroxo bridges), which

indicates that the spin-polarization mechanism is the dominant pathway responsible for the observed antiferromagnetic interactions in complex **1**.

To further understand the differences in the observed J_1 - J_3 values, here we have modeled three dimeric complexes by replacing the other two Gd^{III} ions with diamagnetic Lu^{III}. The dinuclear model complexes M₁, M₂, and M₃ correspond to the J_1 , J_2 , and J_3 interactions present in complex **1** (see Scheme 1). The computed J values for the M₁ and M₃ model complexes (corresponding to the J_1 and J_3 interaction in **1**) are -0.18 and -0.19 cm⁻¹, respectively. Although the computed J values are quite large compared to pairwise extracted J values in the parent complex, our model complex indicates that the J_1 and J_3 interactions are of comparable magnitude. This is further corroborated by computed overlap integrals between corresponding 4*f* orbitals, where both M₁ and M₃ have nearly similar overlap integral values. On the other hand, our model complex M₂ shows the J value of -0.06 cm⁻¹, much smaller than the J 's obtained for the M₁ and M₃ model complexes. Calculations on dimer complexes nicely reflect the observed trends in the J values obtained for the polynuclear complexes. Among dinuclear/polynuclear lanthanides complexes, the ∠Gd-O-Gd bond angle is observed to be the most influential parameter that dictates the nature of the magnetic interaction. Previous magneto-structural correlation studies suggest that a large ∠Gd-O-Gd bond angle (> 110°) often results in a weak ferromagnetic exchange.^{128, 135-138}

For J_1 interaction, the ∠Gd-O-Gd bond angle for μ₂-O bridge is ~108° and 105°/100° (avg. ~ 102.5°) degree for η²- bridged peroxo ligand. Contrarily, the body-body interaction J_3 emerges from the two η²- bridged peroxo ligand having an avg. ∠Gd-O-Gd bond angle ~98°. The avg. ∠Gd-O-Gd bond angle for J_1 and J_3 interactions are ~104° and 98°, respectively. This small variation in the ∠Gd-O-Gd bond angle is reflected in the computed J values, where J_3 is marginally large in magnitude compared to the J_1 interaction. On the other hand, our model

complex M_2 shows the value of -0.06 cm^{-1} , much smaller than the J 's obtained for the M_1 and M_3 model complexes. The avg. $\angle\text{Gd-O-Gd}$ bond angle in the M_2 complex is $\sim 128^\circ$ degrees, much larger than the average bond angle observed for M_1 and M_3 complexes. As a result of the large bond angles, the ferromagnetic contributions to the total J value increase due to the enhanced charge transfer mechanism through the vacant 5d-orbitals.¹³⁵ Moreover, we have also observed strong $4f$ - $4f$ overlap integral values for M_2 model complexes, highlighting the enhanced antiferromagnetic interaction contributions to the J values (see Figure 7). These two competing interactions in the M_3 model complex results in a weak antiferromagnetic J value. We have not discussed J_4 interaction using the model complex as it is very weak and insensitive towards fitting the magnetic susceptibility.

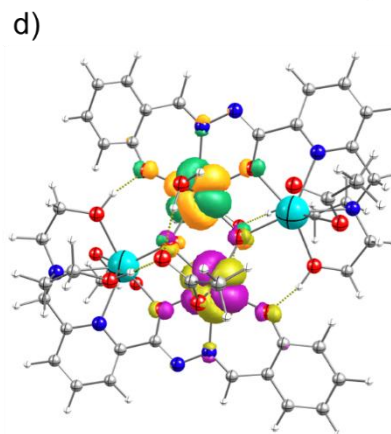
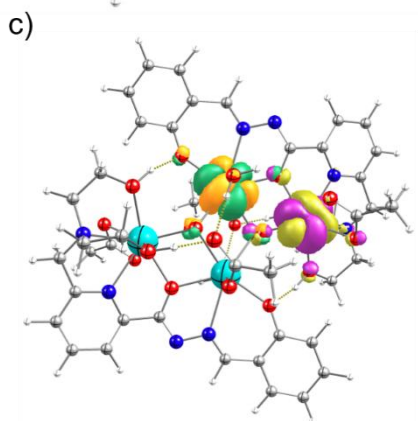
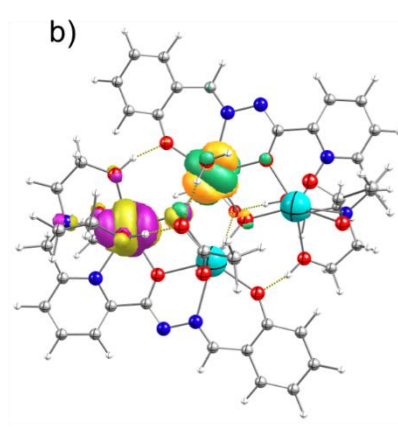
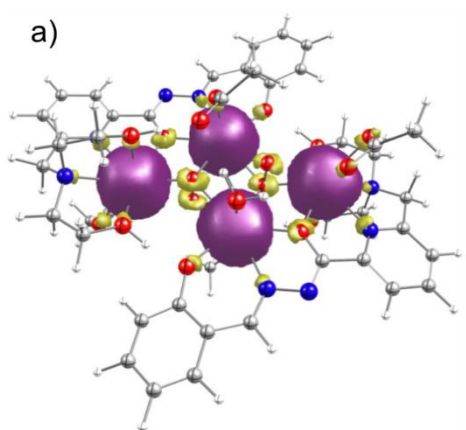


Figure 7. a) DFT computed spin-density of the high-spin state ($S = 14$) of the complex **1** along with the strongest overlap between corresponding orbitals for b) J_2 interaction; c) J_1 interaction, and d) J_3 interaction. Spin-density plot is constructed with an iso-value of $0.001 \text{ e}^-/\text{bohr}^3$, where the violet and yellow color represents the positive and negative spin-densities. Color code: Gd (cyan), O (red), N (blue), C(grey), and H (white)

In the next step, we have analysed the MCE properties of complex **1** using DFT computed J values. For complex **1**, the maximum change in the entropy is $\Delta S_m(T)$ is $\sim 33.60 \text{ J K}^{-1} \text{ Kg}^{-1}$ at 4 K and $\Delta H = 13.0 \text{ T}$. The experimentally observed $\Delta S_m(T)$ values are very close to the theoretical limit value of $36.165 \text{ J K}^{-1} \text{ Kg}^{-1}$ obtained from the uncoupled four Gd(III) ions using the following expression ($\Delta S = nR \ln(2S + 1)/M_w$; where R is the gas constant, n the number of non-interacting spins (4), $S = 7/2$, and $M_w = 1912.287 \text{ g/mol}$). Such closeness between the theoretical and computed $\Delta S_m(T)$ value indicates the presence of the multiple low-lying excited states. Using DFT calculated J values, we have computed the relative energies of all the possible spin-states through diagonalization of the spin-Hamiltonian. The eigenvalue plot of all the possible spin states for complex **1** is provided in Figure 8. The computed eigenvalue plot indicates the presence of several hundred states (\sim continuum) within the energy range of $\sim 1 \text{ cm}^{-1}$, emerging from multiple weak competing Gd^{III}-Gd^{III} interactions present in complex **1** (see Figure 8a). The continuum of all states explains why the experimentally observed $\Delta S_m(T)$ is much closer to the theoretical value. Due to highly demanding MCE simulations with four Gd^{III} centres ($S = 7/2$), we have simulated the $-\Delta S_m(T)$ vs. T using the dimeric model complexes (as the Gd₄O₆ core is formed by bridging two dinuclear subunits). The computed $-\Delta S_m$ value for the dimeric unit with J_1 interaction yields a maximum of $34.45 \text{ J K}^{-1} \text{ Kg}^{-1}$ at 4 K and $\Delta H = 13.0 \text{ T}$.

The computed value for the dimeric model is very close to the observed experimental value $\sim 33.60 \text{ J K}^{-1} \text{ Kg}^{-1}$. The minor difference in the observed $-\Delta S_m$ values for different model complexes is directly related to the difference in the strength of the magnetic exchange interactions (see Figure S30). Moreover, the strong dependence of the MCE at low temperatures implies a continuum of the low-lying excited states emerging from the weakly coupled Gd^{III} centres (see Figure 8a).

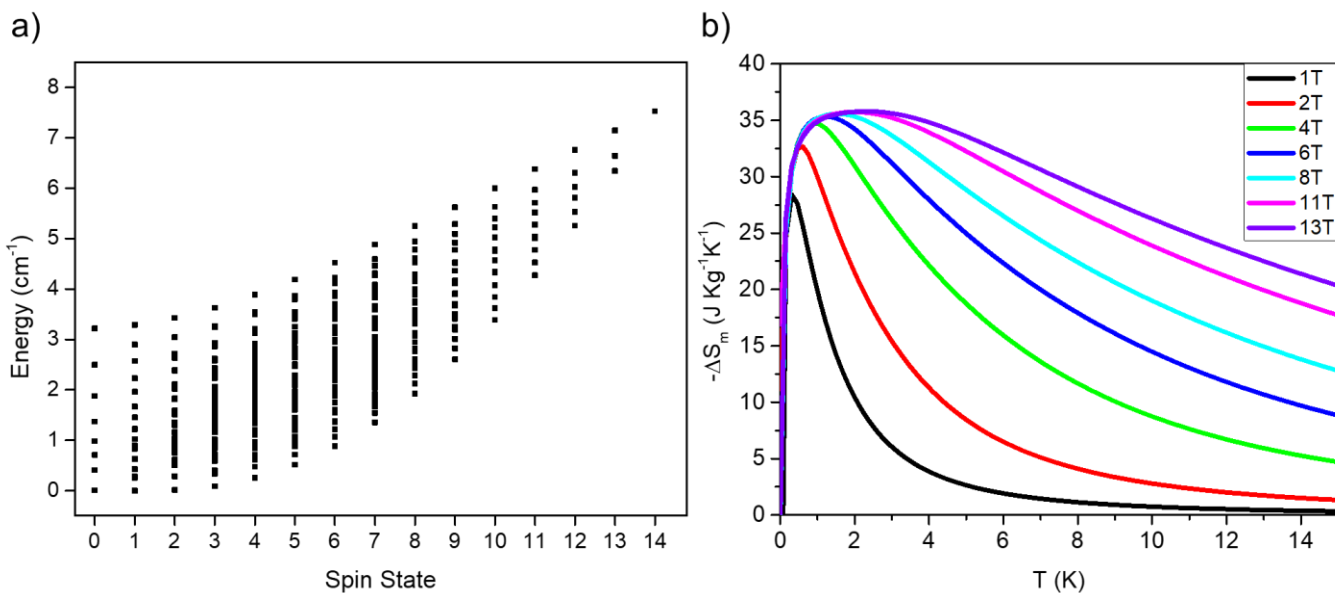


Figure 8. a) DFT computed eigen value plot of all the spin states for **1** derived from the computed J values; b) DFT simulated $-\Delta S_m$ versus T plot using dimeric model complex.

Single-Ion Anisotropy in Complexes 2-4

To understand the electronic structure and probe the origin of magnetic anisotropy in complexes **2-4**, we have carried out CASSCF calculations on the individual paramagnetic ions of each complex (see computational methodology for details). Based on the local coordination environment around Ln^{III} ions, we have observed that there are two distinct Ln^{III} ions possessing an N₃O₆ environment in a spherical capped square antiprism and an N₂O₇ coordination environment in a muffin geometry.

For complex **2**, we have computed all the septet and quintet states and mixed them using the RASSI-SO module to get the spin-orbit states of all the individual centres. The SOC spectrum of the ground state ⁷F₆ comprising thirteen states spans over an energy range of the ~286 (~345) cm⁻¹ for Tb@1/Tb@3 (Tb@2/Tb@4) centres, respectively (see Tables S21-S24). The ground state g-tensor shows Ising type anisotropy with *g_{zz}* value of 17.186 (17.720) for Tb@1/Tb@3 (Tb@2/Tb@4) centres (see Tables S31-S32). For both the Tb@1/Tb@3 (Tb@2/Tb@4) centres, the ground state g-tensor does not lie in the molecular plane and is oriented towards the μ₂-O bridges connecting the two Tb^{III} atoms. Wavefunction decomposition analysis suggests stabilization of the |±6⟩ state as the ground state for both the Tb@1/Tb@3 (Tb@2/Tb@4) centres with little admixing from other excited states (See Tables 4 and S39). The non-collinearity in the ground and excited *g_{zz}* indicate that the magnetic relaxation is likely to occur through the first excited KD. This is further supported by the observed large tunnel splitting value (0.7 for Tb@1/Tb@3 while 0.3 for Tb@2/Tb@4) between the first excited pseudo-KDs, indicating magnetic relaxation occurs via this state. Our calculations predict the theoretical barrier height to be ~77.4 (116.2) cm⁻¹ for the Tb@1/Tb@3 (Tb@2/Tb@4) centres. We have also noticed a significantly large tunnel splitting value of 0.7 (0.3) cm⁻¹ between the ground state pseudo-KDs

of the Tb@1/Tb@3 (Tb@2/Tb@4) centres. This tunnel splitting value is the direct measure of the extent of the QTM within the ground state of non-Kramer type Tb^{III} ion. Additionally, the computed crystal field parameters indicate comparable axial and non-axial parameters for both the Tb@1/Tb@3 (Tb@2/Tb@4) centres, suggesting that the ligand field fails to provide a complete axial ligand field environment for oblate type Tb^{III} ion (see Table S36).

For complex **3**, we have computed 21 sextet states for individual ions, and CASSCF computed spectrum spanned over an energy range of ~ 34952 (34989) cm^{-1} with the first excited spin-free state located at ~ 31 (18) cm^{-1} for Dy@1/Dy@3 (Dy@2/Dy@4) sites. RASSI-SO computed energy spectrum of the spin-orbit states for Dy@1/Dy@3 and Dy@2/Dy@4 sites are over 355 cm^{-1} and 391 cm^{-1} , respectively (see Tables S17-S20). The computed ground state g-values are $g_{xx} = 0.266$, $g_{yy} = 0.394$, $g_{zz} = 18.854$ and $g_{xx} = 0.2228$, $g_{yy} = 0.367$, $g_{zz} = 17.014$ for Dy@1/Dy@3 and Dy@2/Dy@4 sites respectively (see Tables S29-S30). The computed g-values are axial. However, they lack pure Ising type anisotropy ($g_{xx} \approx g_{yy} \approx 0$; $g_{zz} \approx 20$), which is the utmost requirement for achieving a highly anisotropic ground state. A wavefunction decomposition analysis indicates the stabilization of the m_J $|\pm 15/2\rangle$ and $|\pm 13/2\rangle$ for Dy@1/Dy@3 and Dy@2/Dy@4 sites, respectively, with admixing from the other higher excited states, resulting in a large transverse component in the g-values (See Tables 4 and S38). Although we notice similarities in the computed energy spectrum for nine coordination Dy sites, the difference in the donor atoms (NO₈ vs. N₂O₇) and local distortion around Dy^{III} centre (spherical capped square antiprism vs. muffin type) lead to the isolation of different magnetic ground states for Dy@1/Dy@3 and Dy@2/Dy@4 sites respectively (see Table S29-S30 for details). The ground state g_{zz} orientation for the Dy@1/Dy@3 sites lies in the molecular plane and passes through the centre of the bridging peroxide ion (see Figure 9). Contrarily, for

Dy@2/Dy@4 sites, the g_{zz} orientation is deviated from the plane of the molecule and oriented toward one of the coordinated Dy-N bonds ($\sim 5.6^\circ$ degrees from the bond). For both the sites, the first excited g-values are $g_{xx} = 0.734$, $g_{yy} = 1.136$, $g_{zz} = 17.299$ (for Dy@1/Dy@3) and $g_{xx} = 0.832$, $g_{yy} = 0.947$, $g_{zz} = 14.471$ (for Dy@2/Dy@4 sites), indicating the presence of significant transverse component in the g-values. The energy of the first excited KD is located at $\sim 76 \text{ cm}^{-1}$ (Dy@1/Dy@3) and 68 cm^{-1} (Dy@2/Dy@4) from the ground state, while the angle between the g_{zz} of the ground and first KD lies between $22\text{-}80^\circ$ for both sites. This indicates that the magnetic relaxation is likely operative via the first excited KD for all the four Dy centres. We have constructed the ab initio blockade barrier to understand the magnetic relaxation by computing the transverse magnetic moments between the KDs. The computed transverse magnetic moment between the ground doublet is 0.10 (0.09) for the Dy@1/Dy@3 and Dy@2/Dy@4 sites, respectively (see Figure S31), which is significantly large to quench the ground state QTM ($\sim 1 \times 10^{-6}$ for complete quenching).^{14,17,139-146} On the other hand, the transverse magnetic moment between the ground and first excited KD is relatively large compared to the number connecting ground doublet, indicating that TA-QTM via first excited KD is a favourable pathway for magnetic relaxation. The computed crystal field parameters indicate that the non-axial B_k^q parameters (where $k = 2, 4$ and 6 and $q \neq 0$) are relatively higher compared to the axial B_k^q terms (where $k = 2, 4$, and 6 and $q = 0$) for both the Dy@1/Dy@3 and Dy@2/Dy@4 sites, indicating the lack of a complete axial ligand field environment offered by both the spherical capped square antiprism and muffin type geometry (see Table S35). Our calculations set the theoretical barrier height of 76 cm^{-1} and 68 cm^{-1} for magnetization relaxation for Dy@1/Dy@3 and Dy@2/Dy@4 sites, respectively, along with dominant QTM within the ground state for complex **3** (see Figure

9). The small energy gap between the first two KDs and dominant QTM within the ground state ensure a lack of single-ion slow relaxation in complex **3**.

For complex **4**, we have computed 35 quartets and 112 doublets for the individual Er^{III} ions. The CASSCF computed quartet state spans over an energy range of ~ 46928 (46976) cm^{-1} with the first excited spin-free state located at ~ 70 (52) cm^{-1} for Er@1/Er@3 (Er@2/Er@4) sites. RASSI-SO computed sixteen SOC states corresponding to the $^4I_{15/2}$ ground state term spans over an energy range of ~ 327 (391) cm^{-1} for Er@1/Er@3 (Er@2/Er@4) sites (see Tables S25-S28). The computed g -values for the ground state KD are $g_{xx} = 2.583$, $g_{yy} = 4.134$, $g_{zz} = 11.954$ (for Er@1/Er@3 sites) and $g_{xx} = 1.558$, $g_{yy} = 2.254$, $g_{zz} = 13.289$ (for Er@2/Er@4 sites), indicating the lack of complete axial g -values (see Table 4). Wavefunction decomposition analysis suggests that the ground state composition is $39.8\% |\pm 15/2\rangle + 32.4\% |\pm 11/2\rangle$ for Er@1/Er@3 sites and $80.0\% |\pm 13/2\rangle$ for Er@2/Er@4 sites, indicating a highly mixed ground state (See Tables 4 and S40). Such large transverse anisotropy in the g -values indicates that the ligand field environment is completely unsuitable to offer axially to the g -values for prolate type Er^{III} ions. The computed CF parameters further support this where the axial B_2^0 term is positive in nature for all the sites and is either comparable or smaller compared to the non-axial terms (where $k = 2, 4$ and 6 and $q \neq 0$) (See Table S37). The first excited KD is primarily $m_J |\pm 1/2\rangle$ in nature for both sites and is located at ~ 40.6 (25.1) cm^{-1} for Er@1/Er@3 and Er@2/Er@4 sites, respectively. The computed ab initio blockade barrier indicates the presence of a large transverse magnetic moment connecting the ground doublet for Er@1/Er@3 sites (1.1) and Er@2/Er@4 sites (0.63) sites (See Figure S32). The computed ground state connecting values are either comparable/marginally small compared to the values connecting the ground and first excited KD, indicating QTM to be the most prominent pathway for magnetic relaxation in complex **4**. Our single-ion anisotropy

analysis suggests that the spherical capped square antiprism/muffin-type geometry around prolate type Er^{III} ion is completely unsuitable for isolating $m_J |\pm 15/2\rangle$ required for achieving slow relaxation.

Table 4. SINGLE_ANISO computed ground state g-tensors, tunnel splitting values, and m_J

Complexes/centers	$g_{xx}; g_{yy}; g_{zz}$	$k_{QT}/\Delta_{\text{tun}} (\text{cm}^{-1})$	U_{eff}	$ \pm m_J\rangle$	
2	Tb1/Tb3	0.000; 0.000; 17.186	0.7	77.4	91.9% $ \pm 6\rangle$
	Tb2/Tb4	0.000; 0.000; 17.720	0.3	116.2	97.0% $ \pm 6\rangle$
3	Dy1/Dy3	0.266; 0.394; 18.854	0.10	75.7	87.9% $ \pm 15/2\rangle$
	Dy2/Dy4	0.229; 0.368; 17.015	0.09	68.3	93.9% $ \pm 13/2\rangle$
	Er1/Er3	2.583; 4.134; 11.954	1.1	40.6	39.8% $ \pm 15/2\rangle$
4					32.4% $ \pm 11/2\rangle$
	Er2/Er4	1.565; 2.274; 13.295	0.63	25.1	80.0% $ \pm 13/2\rangle$

composition and theoretical U_{cal} values for complexes **2-4**.

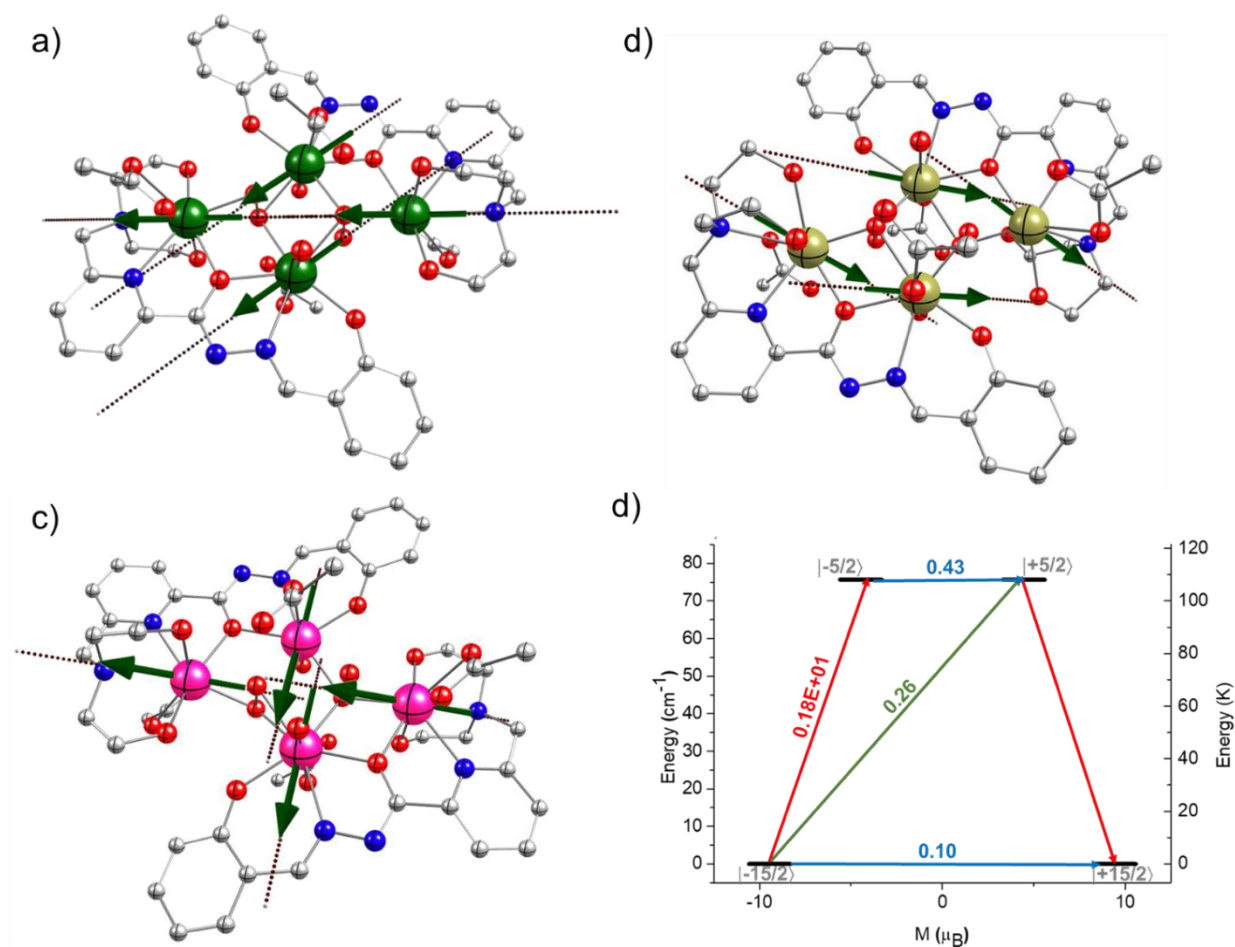


Figure 9. SINGLE_ANISO computed orientation of the ground state main magnetic axis (g_{zz}) of the individual centres in a) complex **3**; b) complex **2** and c) complex **4** along with ab initio blockade barrier for Dy@1/Dy@3 sites in complex **1**. Colour code: Dy (green), Tb (olive), Er (pink), O (red), N (blue), C (grey). The hydrogen atoms are omitted for clarity.

To further investigate the nature and magnitude of magnetic interactions present in anisotropic complexes **2-4**, here we have simulated the static DC magnetic data (magnetic susceptibility and magnetization) using the POLY_ANISO code implemented in the Open MOLCAS code.⁷²⁻⁷³ Here, we have used the CASSCF computed SINGLE_ANISO data of the individual paramagnetic centres as an input for the simulations. This methodology utilizes the Lines Model

to extract the magnetic exchange interaction between different Ln^{III} centres and the dipole-dipole contributions to the total exchange. As observed for complex **1** (from DFT calculations), we have considered three different exchange interactions (J_1 , J_2 , and J_3) to simulate the magnetic susceptibility and magnetization data. The simulation nicely reproduces the experimentally observed trend for all the complexes **2-4** (Figures 4 and S33). For complex **3**, the best fit yields J_{tot} ($J_1 = +0.1 \text{ cm}^{-1}$, $J_2 = +0.05 \text{ cm}^{-1}$ and $J_3 = +0.35 \text{ cm}^{-1}$) a ferromagnetic interaction between the respective Dy^{III} centres. Both the exchange and the dipolar contributions are ferromagnetic in nature for all three interactions (see Table 5). From Table 5, it is evident that the exchange contributions dominate in J_1 and J_3 interactions while dipolar contributions dominate in the J_2 interactions. This is in line with DFT analysis on **1**, which predicts stronger exchange for the J_1 and J_3 interaction while weak exchange interaction for J_2 interactions. On the other hand, the best fit yields (J_{tot}) $J_1 = -0.08 \text{ cm}^{-1}$, $J_2 = -0.007 \text{ cm}^{-1}$ and $J_3 = -0.12 \text{ cm}^{-1}$ for complex **2** and $J_1 = -0.10 \text{ cm}^{-1}$, $J_2 = -0.005 \text{ cm}^{-1}$ and $J_3 = -0.30 \text{ cm}^{-1}$ for complex **4**.

Table 5. Magnetic Exchange Coupling J estimated from the POLY_ANISO simulation of dc data for complexes **2-4**.

Complex	J_{tot} $J_1/J_2/J_3$	J_{ex} $J_1/J_2/J_3$	J_{dipo} $J_1/J_2/J_3$
2	-0.08/-0.007/-0.12	-0.1/-0.007/-0.15	0.02/0.003/0.03
3	0.1/0.05/0.35	0.08/0.01/0.30	0.02/0.04/0.05
4	-0.1/-0.005/-0.30	-0.15/-0.008/-0.40	0.5/0.003/0.10

The low-lying magnetic exchange spectrum and tunnelling gap (Δ_{tun}) between the doublets generated during the simulation of dc data of complexes **2-4** are reported in Table S43-S45 in ESI. The exchange energy states span up to 73.44 cm^{-1} (Table S43 and Figure 10) for complex **3**. The tunnelling gap between the ground exchange state doublet $3.7\text{E-}08 \text{ cm}^{-1}$ is very small,

indicating negligible QTM within the ground state. A similar picture has been observed for the first and second excited states located at 2.7 cm^{-1} higher in energy from the ground state. The extent of the tunnel splitting increases dramatically from the third excited exchange state onwards ($\approx 10^{-6}$), indicating the presence of a thermal-assisted QTM via these states. Here, we have observed eight low-lying exchange doublets within the narrow energy range of $\sim 7.7 \text{ cm}^{-1}$, while the other excited exchange states are much higher in energy. The obtained exchange spectrum analysis indicates that the magnetic relaxation is likely to occur via the eight excited KD as it is difficult to populate higher energy states at low temperatures. In our experimental finding no well resolved zero-field out-of-phase magnetic susceptibility signals were observed for **3** which is consistent with the low theoretical energy barrier of only 7.7 cm^{-1} (11 K). The application of a small dc magnetic field (1 kOe) suppressed the tunnelling process between the magnetic exchange states and resolves the out-of-phase signals to reach the experimental energy barrier of 23 K for the spin reversal for **3**. In the cases of complexes **2**, and **4**, no out-of-phase magnetic susceptibility signals were observed, which are well rationalized with the theoretical finding. As can be seen from Tables S44 and S45 a tunnelling gap $\approx 10^{-2} \text{ cm}^{-1}$ between the ground exchange state was found in both complexes **2** and **4**, which suggests fast magnetic relaxation between ground-state doublet and denies any possibility of zero-field SMM behaviour which is further rationalized with the absence of a zero-field out-of-phase magnetic relaxation in the experiment.

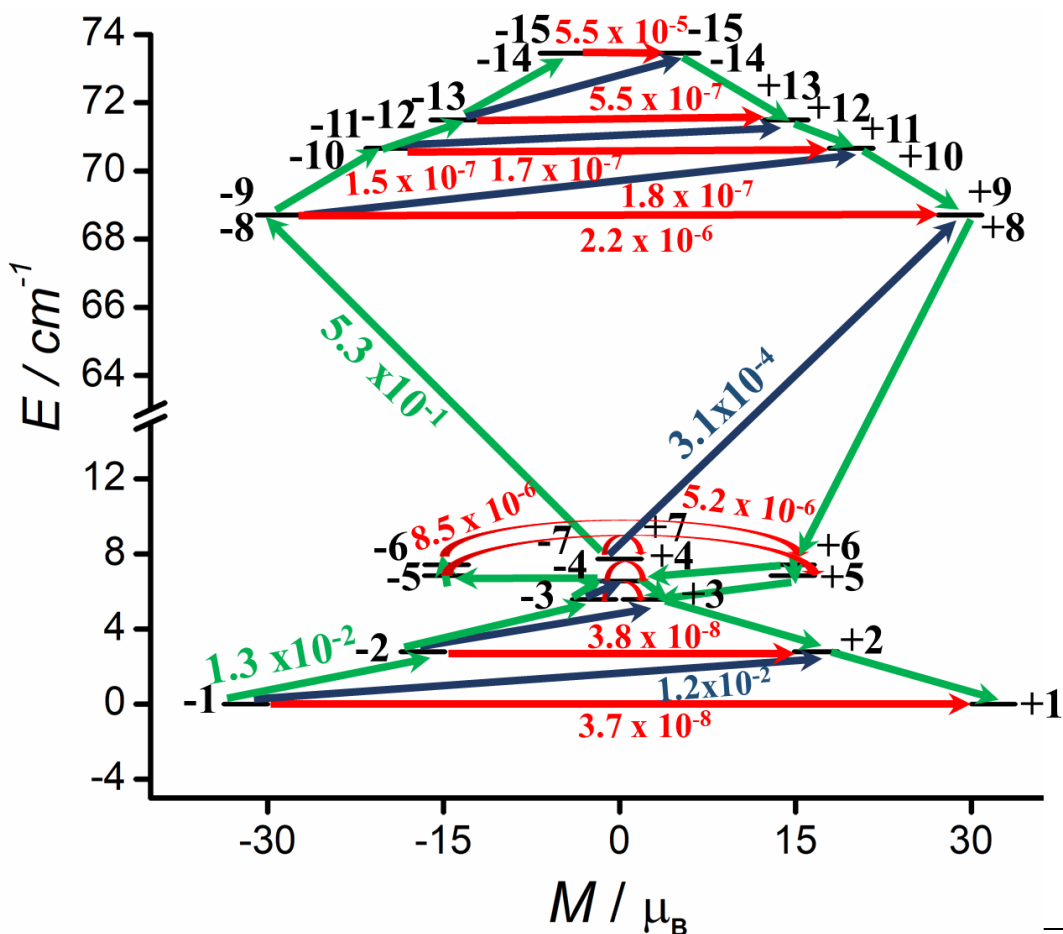


Figure 10. Magnetic relaxation between exchange states in complex 3. The red arrows and values represent the tunnelling gap between exchange states, while the blue and green arrows and values represent Orbach/Raman and Orbach magnetic relaxations.

Conclusion

In summary, we have synthesized a series of tetranuclear assemblies supported by peroxide ligand, which binds to metals centres in a side-on manner using the coordination mode $\mu_3\text{-}\eta^2\text{:}\eta^2\text{:}\eta^2$. Overall, the tetranuclear complexes contain two types of nine coordinated metal centres with different coordination environments; one in an N_3O_6 environment with spherical capped square antiprism geometry while the other is in an N_2O_7 coordination environment with muffin geometry. All the complexes show weak antiferromagnetic interactions except 3, which reveals

weak ferromagnetic interactions. Due to the isotropic nature of Gd^{III} ions and weak antiferromagnetic interactions between them in **1**, a magnetocaloric effect is observed with the maximum value of $-\Delta S_m = 33.60 \text{ J kg}^{-1} \text{ K}^{-1}$ at $T = 4 \text{ K}$, $\Delta H = 13 \text{ T}$. The ac susceptibility measurements reveal that complex **3** at 1kOe shows two different relaxation events; a low frequency (LF) contribution with fitted parameters, $U_{\text{eff}} = 23(2) \text{ K}$, $\tau_0 = 9(2) \cdot 10^{-7} \text{ s}$, $C = 187(99) \text{ K}^{-n} \text{ s}^{-1}$ and $n = 1.7(7)$, by the contribution of Orbach and Raman processes and a high frequency (HF) contribution with fitted parameter, $A = 3.18(7) \cdot 10^{-8} \text{ Oe}^{-4} \cdot \text{K}^{-1} \text{ s}^{-1}$, driven by direct process. In **4**, the relaxation is purely driven by the direct process with $A = 1.56(2) \cdot 10^{-13} \text{ Oe}^{-4} \text{ K}^{-1} \text{ s}^{-1}$. The experimental finding of the magnetic and magnetothermal properties was further fully rationalized with detailed theoretical studies.

Electronic Supplementary Information (ESI): Peroxo binding modes, Simulated single-crystal data and experimental XRD pattern for **1-4**, TGA curves for **1-4**, Continuous Shape measurement calculations, Molecular structure, and Supramolecular interactions of **1-4**, Frequency dependence of the in-phase (χ_M') and out-of-phase (χ_M'') components of the ac susceptibility measured on powder at 2 K from 0 to 3 kOe for **2-4**, Field dependence of the relaxation time of the magnetization at 2 K for **3** (full and empty black circles) and **4** (green circles), Frequency dependence of the in-phase (χ_M') and out-of-phase (χ_M'') components of the magnetic susceptibility of **4** in 4 kOe external field and from 2 to 12 K, and BS-DFT computed energies of high-spin and broken-symmetry solution of Gd_4 , DFT computed corresponding orbitals for which the overlap integral values were calculated for model 3 equivalent to J_I interaction of complex **1** at contour value = $0.03 \text{ e}^-/\text{bohr}^3$, Simulation of DC magnetic susceptibility and magnetization (at 2 K) data using the DFT computed J values. Solid red lines represent the simulated data.

AUTHOR INFORMATION

Corresponding Authors

*E-mail: vc@iitk.ac.in.

* Email: fabrice.pointillart@univ-rennes1.fr

*E-mail: sksingh@chy.iith.ac.in

ORCID

Vadapalli Chandrasekhar: ORCID: 0000-0003-1968-2980

Fabrice Pointillart: ORCID: 0000-0001-7601-1927

Saurabh Kumar Singh: ORCID: 0000-0001-9488-8036

Prem Prakash Sahu: ORCID: 0000-0002-8645-2483

‡ Authors contributed equally

Notes

The authors declare no competing financial interest.

ACKNOWLEDGEMENTS

We thank the Department of Science and Technology (DST), India; and support for the Single Crystal CCD X-ray Diffractometer facility at IIT-Kanpur. V.C. is grateful to the DST for a J. C. Bose fellowship. P.K. thanks University Grants Commission (UGC), India, for Senior Research Fellowship. S.K.S and P.P.S acknowledge the Department of Science and Technology for the Start-up Research Grant (SRG/2020/001323). S.K.S. thanks IIT Hyderabad for generous seed grant funding. The support and resources provided by PARAM Shivay Facility under the National Supercomputing Mission, Government of India at the Indian Institute of Technology, Varanasi, are gratefully acknowledged.

References

1. T.-Q. Song, J. Dong, A.-F. Yang, X.-J. Che, H.-L. Gao, J.-Z. Cui and B. Zhao, Wheel-like Ln_{18} Cluster Organic Frameworks for Magnetic Refrigeration and Conversion of CO_2 , *Inorg. Chem.*, 2018, **57**, 3144-3150.
2. P. W. Roesky and T. E. Müller, Enantioselective Catalytic Hydroamination of Alkenes, *Angew. Chem. Int. Ed.*, 2003, **42**, 2708-2710.
3. F. Pohlki and S. Doye, The catalytic hydroamination of alkynes, *Chem. Soc. Rev.*, 2003, **32**, 104-114.
4. R. Sessoli and A. K. Powell, Strategies towards single molecule magnets based on lanthanide ions, *Coord. Chem. Rev.*, 2009, **253**, 2328-2341.
5. H. L. C. Feltham and S. Brooker, Review of purely 4f and mixed-metal nd-4f single-molecule magnets containing only one lanthanide ion, *Coord. Chem. Rev.*, 2014, **276**, 1-33.
6. A. Dey, P. Kalita and V. Chandrasekhar, Lanthanide(III)-Based Single-Ion Magnets, *ACS Omega*, 2018, **3**, 9462-9475.
7. Z. Zhu, M. Guo, X.-L. Li and J. Tang, Molecular magnetism of lanthanide: Advances and perspectives, *Coord. Chem. Rev.*, 2019, **378**, 350-364.
8. E. Coronado, Molecular magnetism: from chemical design to spin control in molecules, materials and devices, *Nature Rev. Mater.*, 2020, **5**, 87-104.
9. S. V. Eliseeva and J.-C. G. Bünzli, Lanthanide luminescence for functional materials and bio-sciences, *Chem. Soc. Rev.*, 2010, **39**, 189-227.
10. M. C. Heffern, L. M. Matosziuk and T. J. Meade, Lanthanide Probes for Bioresponsive Imaging, *Chem. Rev.*, 2014, **114**, 4496-4539.

11. N. Ishikawa, M. Sugita, T. Ishikawa, S.-y. Koshihara and Y. Kaizu, Lanthanide Double-Decker Complexes Functioning as Magnets at the Single-Molecular Level, *J. Am. Chem. Soc.*, 2003, **125**, 8694-8695.
12. S. K. Gupta, T. Rajeshkumar, G. Rajaraman and R. Murugavel, An air-stable Dy(III) single-ion magnet with high anisotropy barrier and blocking temperature, *Chem. Sci.*, 2016, **7**, 5181-5191.
13. J. Liu, Y.-C. Chen, J.-L. Liu, V. Vieru, L. Ungur, J.-H. Jia, L. F. Chibotaru, Y. Lan, W. Wernsdorfer, S. Gao, X.-M. Chen and M.-L. Tong, A Stable Pentagonal Bipyramidal Dy(III) Single-Ion Magnet with a Record Magnetization Reversal Barrier over 1000 K, *J. Am. Chem. Soc.*, 2016, **138**, 5441-5450.
14. C. A. P. Goodwin, F. Ortu, D. Reta, N. F. Chilton and D. P. Mills, Molecular magnetic hysteresis at 60 kelvin in dysprosocenium, *Nature*, 2017, **548**, 439-442.
15. J. Lu, M. Guo and J. Tang, Recent Developments in Lanthanide Single-Molecule Magnets, *Chem. Asian J.*, 2017, **12**, 2772-2779.
16. M. Feng and M.-L. Tong, Single Ion Magnets from 3d to 5f: Developments and Strategies, *Chem. Eur. J.*, 2018, **24**, 7574-7594.
17. F.-S. Guo, M. Day Benjamin, Y.-C. Chen, M.-L. Tong, A. Mansikkamäki and A. Layfield Richard, Magnetic hysteresis up to 80 kelvin in a dysprosium metallocene single-molecule magnet, *Science*, 2018, **362**, 1400-1403.
18. J.-L. Liu, Y.-C. Chen and M.-L. Tong, Symmetry strategies for high performance lanthanide-based single-molecule magnets, *Chem. Soc. Rev.*, 2018, **47**, 2431-2453.
19. K. L. M. Harriman, D. Errulat and M. Murugesu, Magnetic Axiality: Design Principles from Molecules to Materials, *Trends Chem.*, 2019, **1**, 425-439.

20. X. Meng, M. Wang, X. Gou, W. Lan, K. Jia, Y.-X. Wang, Y.-Q. Zhang, W. Shi and P. Cheng, Two C_{2v} symmetry dysprosium(iii) single-molecule magnets with effective energy barriers over 600 K, *Inorg. Chem. Front.*, 2021, **8**, 2349-2355.
21. S.-D. Jiang, B.-W. Wang, H.-L. Sun, Z.-M. Wang and S. Gao, An Organometallic Single-Ion Magnet, *J. Am. Chem. Soc.*, 2011, **133**, 4730-4733.
22. M. Evangelisti and E. K. Brechin, Recipes for enhanced molecular cooling, *Dalton Trans.*, 2010, **39**, 4672-4676.
23. G. Lorusso, M. A. Palacios, G. S. Nichol, E. K. Brechin, O. Roubeau and M. Evangelisti, Increasing the dimensionality of cryogenic molecular coolers: Gd-based polymers and metal-organic frameworks, *Chem. Commun.*, 2012, **48**, 7592-7594.
24. R. Sessoli, Chilling with Magnetic Molecules, *Angew. Chem. Int. Ed.*, 2012, **51**, 43-45.
25. Y.-Z. Zheng, G.-J. Zhou, Z. Zheng and R. E. P. Winpenny, Molecule-based magnetic coolers, *Chem. Soc. Rev.*, 2014, **43**, 1462-1475.
26. J.-L. Liu, Y.-C. Chen, F.-S. Guo and M.-L. Tong, Recent advances in the design of magnetic molecules for use as cryogenic magnetic coolants, *Coord. Chem. Rev.*, 2014, **281**, 26-49.
27. Y. Han, S.-D. Han, J. Pan, Y.-J. Ma and G.-M. Wang, An excellent cryogenic magnetic cooler: magnetic and magnetocaloric study of an inorganic frame material, *Mater. Chem. Front.*, 2018, **2**, 2327-2332.
28. S.-J. Liu, S.-D. Han, J.-P. Zhao, J. Xu and X.-H. Bu, In-situ synthesis of molecular magnetorefrigerant materials, *Coord. Chem. Rev.*, 2019, **394**, 39-52.

29. A. Dey, P. Bag, P. Kalita and V. Chandrasekhar, Heterometallic Cu^{II}-Ln^{III} complexes: Single molecule magnets and magnetic refrigerants, *Coord. Chem. Rev.*, 2021, **432**, 213707.
30. M. Evangelisti, O. Roubeau, E. Palacios, A. Camón, T. N. Hooper, E. K. Brechin and J. J. Alonso, Cryogenic Magnetocaloric Effect in a Ferromagnetic Molecular Dimer, *Angew. Chem. Int. Ed.*, 2011, **50**, 6606-6609.
31. F.-S. Guo, J.-D. Leng, J.-L. Liu, Z.-S. Meng and M.-L. Tong, Polynuclear and Polymeric Gadolinium Acetate Derivatives with Large Magnetocaloric Effect, *Inorg. Chem.*, 2012, **51**, 405-413.
32. L.-X. Chang, G. Xiong, L. Wang, P. Cheng and B. Zhao, A 24-Gd nanocapsule with a large magnetocaloric effect, *Chem. Commun.*, 2013, **49**, 1055-1057.
33. G. Lorusso, J. W. Sharples, E. Palacios, O. Roubeau, E. K. Brechin, R. Sessoli, A. Rossin, F. Tuna, E. J. L. McInnes, D. Collison and M. Evangelisti, A Dense Metal–Organic Framework for Enhanced Magnetic Refrigeration, *Advanced Mater.*, 2013, **25**, 4653-4656
34. O. Roubeau, G. Lorusso, S. J. Teat and M. Evangelisti, Cryogenic magneto-caloric effect and magneto-structural correlations in carboxylate-bridged Gd(III) compounds, *Dalton Trans.*, 2014, **43**, 11502-11509.
35. R. Sibille, E. Didelot, T. Mazet, B. Malaman and M. François, Magnetocaloric effect in gadolinium-oxalate framework Gd₂(C₂O₄)₃(H₂O)₆·(0·6H₂O), *APL Mater.*, 2014, **2**, 124402.

36. Y.-C. Chen, L. Qin, Z.-S. Meng, D.-F. Yang, C. Wu, Z. Fu, Y.-Z. Zheng, J.-L. Liu, R. Tarasenko, M. Orendáč, J. Prokleška, V. Sechovský and M.-L. Tong, Study of a magnetic-cooling material $\text{Gd}(\text{OH})\text{CO}_3$, *J. Mater. Chem. A*, 2014, **2**, 9851-9858.
37. Y.-C. Chen, J. Prokleška, W.-J. Xu, J.-L. Liu, J. Liu, W.-X. Zhang, J.-H. Jia, V. Sechovský and M.-L. Tong, A brilliant cryogenic magnetic coolant: magnetic and magnetocaloric study of ferromagnetically coupled GdF_3 , *J. Mater. Chem. C*, 2015, **3**, 12206-12211.
38. P. J. Saines, J. A. M. Paddison, P. M. M. Thygesen and M. G. Tucker, Searching beyond Gd for magnetocaloric frameworks: magnetic properties and interactions of the $\text{Ln}(\text{HCO}_2)_3$ series, *Mater. Horiz.*, 2015, **2**, 528-535.
39. S. Biswas, A. K. Mondal and S. Konar, Densely Packed Lanthanide Cubane Based 3D Metal–Organic Frameworks for Efficient Magnetic Refrigeration and Slow Magnetic Relaxation, *Inorg. Chem.*, 2016, **55**, 2085-2090.
40. J.-Z. Qiu, Y.-C. Chen, L.-F. Wang, Q.-w. Li, M. Orendáč and M.-L. Tong, The effect of magnetic coupling on magneto-caloric behaviour in two 3D $\text{Gd}(\text{iii})$ –glycolate coordination polymers, *Inorg. Chem. Front.*, 2016, **3**, 150-156.
41. W.-P. Chen, P.-Q. Liao, P.-B. Jin, L. Zhang, B.-K. Ling, S.-C. Wang, Y.-T. Chan, X.-M. Chen and Y.-Z. Zheng, The Gigantic $\{\text{Ni}_{36}\text{Gd}_{102}\}$ Hexagon: A Sulfate-Templated “Star-of-David” for Photocatalytic CO_2 Reduction and Magnetic Cooling, *J. Am. Chem. Soc.*, 2020, **142**, 4663-4670.
42. A. V. Pavlishchuk and V. V. Pavlishchuk, Principles for Creating “Molecular Refrigerators” Derived from Gadolinium(III) Coordination Compounds: A Review, *Theor. Exp. Chem.*, 2020, **56**, 1-25.

43. M. Orts-Arroyo, R. Rabelo, A. Carrasco-Berlanga, N. Moliner, J. Cano, M. Julve, F. Lloret, G. De Munno, R. Ruiz-García, J. Mayans, J. Martínez-Lillo and I. Castro, Field-induced slow magnetic relaxation and magnetocaloric effects in an oxalato-bridged gadolinium(III)-based 2D MOF, *Dalton Trans.*, 2021, **50**, 3801-3805.
44. V. Chandrasekhar, S. Hossain, S. Das, S. Biswas and J.-P. Sutter, Rhombus-Shaped Tetranuclear [Ln₄] Complexes [Ln = Dy(III) and Ho(III)]: Synthesis, Structure, and SMM Behavior, *Inorg. Chem.*, 2013, **52**, 6346-6353.
45. S. Das, S. Hossain, A. Dey, S. Biswas, J.-P. Sutter and V. Chandrasekhar, Molecular Magnets Based on Homometallic Hexanuclear Lanthanide(III) Complexes, *Inorg. Chem.*, 2014, **53**, 5020-5028.
46. S. Biswas, S. Das, T. Gupta, S. K. Singh, M. Pissas, G. Rajaraman and V. Chandrasekhar, Observation of Slow Relaxation and Single-Molecule Toroidal Behavior in a Family of Butterfly-Shaped Ln₄ Complexes, *Chem. Eur. J.*, 2016, **22**, 18532-18550.
47. S. Biswas, S. Das, J. Acharya, V. Kumar, J. van Leusen, P. Kögerler, J. M. Herrera, E. Colacio and V. Chandrasekhar, Homometallic Dy^{III} Complexes of Varying Nuclearity from 2 to 21: Synthesis, Structure, and Magnetism, *Chem. Eur. J.*, 2017, **23**, 5154-5170.
48. J. Acharya, S. Biswas, J. van Leusen, P. Kumar, V. Kumar, R. S. Narayanan, P. Kögerler and V. Chandrasekhar, Exploring Tuning of Structural and Magnetic Properties by Modification of Ancillary β-Diketonate Co-ligands in a Family of Near-Linear Tetranuclear Dy^{III} Complexes, *Crys. Growth Des.*, 2018, **18**, 4004-4016.
49. S. Biswas, P. Kumar, A. Swain, T. Gupta, P. Kalita, S. Kundu, G. Rajaraman and V. Chandrasekhar, Phosphonate-assisted tetranuclear lanthanide assemblies: observation of the toroidal ground state in the Tb^{III} analogue, *Dalton Trans.*, 2019, **48**, 6421-6434.

50. P. Kumar, S. Biswas, A. Swain, J. Acharya, V. Kumar, P. Kalita, J. F. Gonzalez, O. Cador, F. Pointillart, G. Rajaraman and V. Chandrasekhar, Azide-Coordination in Homometallic Dinuclear Lanthanide(III) Complexes Containing Nonequivalent Lanthanide Metal Ions: Zero-Field SMM Behavior in the Dysprosium Analogue, *Inorg. Chem.*, 2021, **60**, 8530-8545.
51. A. I. Vogel, B. S. Furniss, A. J. Hannaford, P. W. G. Smith and A. R. Tatchell, *Vogel's textbook of practical organic chemistry. 5th ed*, Longman, Harlow, 1989.
52. D. B. G. Williams and M. Lawton, Drying of Organic Solvents: Quantitative Evaluation of the Efficiency of Several Desiccants, *J. Org. Chem.*, 2010, **75**, 8351-8354.
53. X. Zeng, D. Coquière, A. Alenda, E. Garrier, T. Prangé, Y. Li, O. Reinaud and I. Jabin, Efficient Synthesis of Calix[6]tmpa: A New Calix[6]azacryptand with Unique Conformational and Host–Guest Properties, *Chem. Eur. J.*, 2006, **12**, 6393-6402.
54. SMART and SAINT, Software Reference manuals, Version 6.45, 2003.
55. G. M. Sheldrick, University of Göttingen: Göttingen, Germany, 2.05 edn., 2002.
56. SHELXTL Reference Manual; Bruker Analytical X-ray Systems, Inc., Madison, WI, 2000.
57. G. Sheldrick, A short history of SHELX, *Acta Crystallogr. Sect. A*, 2008, **64**, 112-122.
58. O. V. Dolomanov, L. J. Bourhis, R. J. Gildea, J. A. K. Howard and H. Puschmann, OLEX2: a complete structure solution, refinement and analysis program, *J. App. Crystallogr.*, 2009, **42**, 339-341.
59. K. Brandenburg, Diamond, version 3.1 e, Crystal Impact GbR: Bonn, Germany, 2005.
60. A. D. Becke, Density-functional exchange-energy approximation with correct asymptotic behavior, *Phys. Rev. A*, 1988, **38**, 3098-3100.

61. J. P. Perdew, Density-functional approximation for the correlation energy of the inhomogeneous electron gas, *Phys. Rev. B*, 1986, **33**, 8822-8824.
62. F. Weigend and R. Hlrichs, Balanced basis sets of split valence, triple zeta valence and quadruple zeta valence quality for H to Rn: Design and assessment of accuracy. *Phys. Chem. Chem. Phys.*, 2005, **7**, 3297-3305.
63. F. Weigend, Accurate Coulomb-fitting basis sets for H to Rn, *Phys. Chem. Chem. Phys.*, 2006, **8**, 1057-1065.
64. F. Neese, Software update: the ORCA program system, version 4.0, *WIREs Comput. Mol. Sc.*, 2018, **8**, e1327.
65. F. Neese, F. Wennmohs, U. Becker and C. Riplinger, The ORCA quantum chemistry program package, *J. Chem. Phys.*, 2020, **152**, 224108.
66. B. A. Hess, Relativistic electronic-structure calculations employing a two-component no-pair formalism with external-field projection operators, *Phys. Rev. A*, 1986, **33**, 3742-3748.
67. A. D. Becke, Density-functional thermochemistry. III. The role of exact exchange, *J. Chem. Phys.*, 1993, **98**, 5648-5652.
68. S. Grimme, J. Antony, S. Ehrlich and H. Krieg, A consistent and accurate ab initio parametrization of density functional dispersion correction (DFT-D) for the 94 elements H-Pu, *J. Chem. Phys.*, 2010, **132**, 154104.
69. S. Grimme, S. Ehrlich and L. Goerigk, Effect of the damping function in dispersion corrected density functional theory, *J. Comput. Chem.*, 2011, **32**, 1456-1465.
70. L. Noodleman, Valence bond description of antiferromagnetic coupling in transition metal dimers, *J. Chem. Phys.*, 1981, **74**, 5737-5743.

71. E. Ruiz, S. Alvarez, A. Rodríguez-Forteza, P. Alemany, Y. Pouillon and C. Massobrio, Electronic Structure and Magnetic Behavior in Polynuclear Transition-Metal Compounds, *Magnetism: Molecules to Materials II*, 2001, DOI: <https://doi.org/10.1002/3527600590.ch7>, 227-279.
72. I. Fdez. Galván, M. Vacher, A. Alavi, C. Angeli, F. Aquilante, J. Autschbach, J. J. Bao, S. I. Bokarev, N. A. Bogdanov, R. K. Carlson, L. F. Chibotaru, J. Creutzberg, N. Dattani, M. G. Delcey, S. S. Dong, A. Dreuw, L. Freitag, L. M. Frutos, L. Gagliardi, F. Gendron, A. Giussani, L. González, G. Grell, M. Guo, C. E. Hoyer, M. Johansson, S. Keller, S. Knecht, G. Kovačević, E. Källman, G. Li Manni, M. Lundberg, Y. Ma, S. Mai, J. P. Malhado, P. Å. Malmqvist, P. Marquetand, S. A. Mewes, J. Norell, M. Olivucci, M. Oppel, Q. M. Phung, K. Pierloot, F. Plasser, M. Reiher, A. M. Sand, I. Schapiro, P. Sharma, C. J. Stein, L. K. Sørensen, D. G. Truhlar, M. Ugandi, L. Ungur, A. Valentini, S. Vancoillie, V. Veryazov, O. Weser, T. A. Wesolowski, P.-O. Widmark, S. Wouters, A. Zech, J. P. Zobel and R. Lindh, OpenMolcas: From Source Code to Insight, *J. Chem. Theory Comput.*, 2019, **15**, 5925-5964.
73. F. Aquilante, J. Autschbach, A. Baiardi, S. Battaglia, V. A. Borin, L. F. Chibotaru, I. Conti, L. De Vico, M. Delcey, I. Fdez. Galván, N. Ferré, L. Freitag, M. Garavelli, X. Gong, S. Knecht, E. D. Larsson, R. Lindh, M. Lundberg, P. Å. Malmqvist, A. Nenov, J. Norell, M. Odelius, M. Olivucci, T. B. Pedersen, L. Pedraza-González, Q. M. Phung, K. Pierloot, M. Reiher, I. Schapiro, J. Segarra-Martí, F. Segatta, L. Seijo, S. Sen, D.-C. Sergentu, C. J. Stein, L. Ungur, M. Vacher, A. Valentini and V. Veryazov, Modern quantum chemistry with [Open]Molcas, *J. Chem. Phys.*, 2020, **152**, 214117.

74. B. O. Roos, P. R. Taylor and P. E. M. Sigbahn, A complete active space SCF method (CASSCF) using a density matrix formulated super-CI approach, *Chem. Phys.*, 1980, **48**, 157-173.
75. B. O. Roos, V. Veryazov and P.-O. Widmark, Relativistic atomic natural orbital type basis sets for the alkaline and alkaline-earth atoms applied to the ground-state potentials for the corresponding dimers, *Theor. Chem. Acc.*, 2004, **111**, 345-351.
76. B. O. Roos, R. Lindh, P.-Å. Malmqvist, V. Veryazov, P.-O. Widmark and A. C. Borin, New Relativistic Atomic Natural Orbital Basis Sets for Lanthanide Atoms with Applications to the Ce Diatom and LuF₃, *J. Phys. Chem. A*, 2008, **112**, 11431-11435.
77. P. Å. Malmqvist, B. O. Roos and B. Schimmelpfennig, The restricted active space (RAS) state interaction approach with spin-orbit coupling, *Chem. Phys. Lett.*, 2002, **357**, 230-240.
78. L. F. Chibotaru and L. Ungur, Ab initio calculation of anisotropic magnetic properties of complexes. I. Unique definition of pseudospin Hamiltonians and their derivation, *J. Chem. Phys.*, 2012, **137**, 064112.
79. L. F. Chibotaru, L. Ungur, C. Aronica, H. Elmol, G. Pilet and D. Luneau, Structure, Magnetism, and Theoretical Study of a Mixed-Valence Co^{II}₃Co^{III}₄ Heptanuclear Wheel: Lack of SMM Behavior despite Negative Magnetic Anisotropy, *J. Am. Chem. Soc.*, 2008, **130**, 12445-12455.
80. L. F. Chibotaru, L. Ungur and A. Soncini, The Origin of Nonmagnetic Kramers Doublets in the Ground State of Dysprosium Triangles: Evidence for a Toroidal Magnetic Moment, *Angew. Chem. Int. Ed.*, 2008, **47**, 4126-4129.

81. L. Ungur, W. Van den Heuvel and L. F. Chibotaru, Ab initio investigation of the non-collinear magnetic structure and the lowest magnetic excitations in dysprosium triangles, *New J. Chem.*, 2009, **33**, 1224-1230.
82. S. Xue, X.-H. Chen, L. Zhao, Y.-N. Guo and J. Tang, Two Bulky-Decorated Triangular Dysprosium Aggregates Conserving Vortex-Spin Structure, *Inorg. Chem.*, 2012, **51**, 13264-13270.
83. Y.-N. Guo, G.-F. Xu, W. Wernsdorfer, L. Ungur, Y. Guo, J. Tang, H.-J. Zhang, L. F. Chibotaru and A. K. Powell, Strong Axiality and Ising Exchange Interaction Suppress Zero-Field Tunneling of Magnetization of an Asymmetric Dy₂ Single-Molecule Magnet, *J. Am. Chem. Soc.*, 2011, **133**, 11948-11951.
84. S. Xue, Y.-N. Guo, L. Zhao, P. Zhang and J. Tang, Unique Y-shaped lanthanide aggregates and single-molecule magnet behaviour for the Dy₄ analogue, *Dalton Trans.*, 2014, **43**, 1564-1570.
85. M. U. Anwar, L. N. Dawe, S. S. Tandon, S. D. Bunge and L. K. Thompson, Polynuclear lanthanide (Ln) complexes of a tri-functional hydrazone ligand – mononuclear (Dy), dinuclear (Yb, Tm), tetranuclear (Gd), and hexanuclear (Gd, Dy, Tb) examples, *Dalton Trans.*, 2013, **42**, 7781-7794.
86. S. Xue, L. Zhao, Y.-N. Guo and J. Tang, A novel windmill-type Dy_{iii} [2 × 2] grid exhibiting slow magnetic relaxation, *Dalton Trans.*, 2012, **41**, 351-353.
87. J. Goura and V. Chandrasekhar, Molecular Metal Phosphonates, *Chem. Rev.*, 2015, **115**, 6854-6965.
88. Cirera, E. Ruiz and S. Alvarez, Continuous Shape Measures as a Stereochemical Tool in Organometallic Chemistry, *Organometallics*, 2005, **24**, 1556-1562.

89. *SHAPE: Continuous Shape Measures calculation 2.1; Electronic Structure Group, Universitat de Barcelona: Spain, 2013*
90. J. T. Miller, Y. Ren, S. Li, K. Tan, G. McCandless, C. Jacob, Z. Wu, C.-W. Chu, B. Lv, M. C. Biewer and M. C. Stefan, Peroxide-Templated Assembly of a Trimetal Neodymium Complex Single-Molecule Magnet, *Inorg. Chem.*, 2020, **59**, 10379-10383.
91. W. J. Gee, J. G. MacLellan, C. M. Forsyth, B. Moubaraki, K. S. Murray, P. C. Andrews and P. C. Junk, Caging Peroxide: Anion-Templated Synthesis and Characterization of a Rare-Earth Cluster, *Inorg. Chem.*, 2012, **51**, 8661-8663.
92. H. Ke, X. Lu, W. Wei, W. Wang, G. Xie and S. Chen, Unusual undecanuclear heterobimetallic Zn_4Ln_7 ($Ln = Gd, Dy$) nano-sized clusters encapsulating two peroxide anions through spontaneous intake of dioxygen, *Dalton Trans.*, 2017, **46**, 8138-8145.
93. C.-M. Liu, D.-Q. Zhang, X. Hao and D.-B. Zhu, Assembly of chiral 3d-4f wheel-like cluster complexes with achiral ligands: single-molecule magnetic behavior and magnetocaloric effect, *Inorg. Chem. Front.*, 2020, **7**, 3340-3351.
94. X.-T. Wang, H.-M. Dong, X.-G. Wang, E.-C. Yang and X.-J. Zhao, Two Oxime-Based $\{Ln^{III}_3Ni^{II}_3\}$ Clusters with Triangular $\{Ln_3(\mu_3-O_2)\}^{7+}$ Core: Solvothermal Syntheses, Crystal Structures, and Magnetic Properties, *Z. Anorg. Allg. Chem.*, 2016, **642**, 1166-1172.
95. D. M. Roitershtein, A. A. Vinogradov, K. A. Lyssenko and I. E. Nifant'ev, Self-assembly of heteroleptic tetranuclear carboxylate complexes of yttrium and lanthanides during hydrolysis and oxidation of rare earth homoleptic carboxylates, *Inorg. Chem. Commun.*, 2017, **84**, 225-228.

96. G. B. Deacon, C. M. Forsyth, D. Freckmann, P. C. Junk, K. Konstas, J. Luu, G. Meyer and D. Werner, Adventitiously Obtained Rare-Earth Peroxide Complexes and Their Structural Characterisation, *Aust. J. Chem.*, 2014, **67**, 1860-1865.
97. O. Kahn, Molecular magnetism, *VCH Publishers, Inc.(USA)*, 1993, 1993, 393.
98. J. P. Costes, F. Dahan, A. Dupuis and J. P. Laurent, A General Route to Strictly Dinuclear Cu(II)/Ln(III) Complexes. Structural Determination and Magnetic Behavior of Two Cu(II)/Gd(III) Complexes, *Inorg. Chem.*, 1997, **36**, 3429-3433.
99. H. B. Callen, Callen, "Thermodynamics and an Introduction to Thermostatistics", 1998, 164-167.
100. X.-Y. Zheng, Y.-H. Jiang, G.-L. Zhuang, D.-P. Liu, H.-G. Liao, X.-J. Kong, L.-S. Long and L.-S. Zheng, A Gigantic Molecular Wheel of {Gd₁₄₀}: A New Member of the Molecular Wheel Family, *J. Am. Chem. Soc.*, 2017, 139, 18178-18181.
101. H.-M. Chen, W.-M. Wang, X.-Q. Li, X.-Y. Chu, Y.-Y. Nie, Z. Liu, S.-X. Huang, H.-Y. Shen, J.-Z. Cui and H.-L. Gao, Luminescence and magnetocaloric effect of Ln₄ clusters (Ln = Eu, Gd, Tb, Er) bridged by CO₃²⁻ deriving from the spontaneous fixation of carbon dioxide in the atmosphere, *Inorg. Chem. Front.*, 2018, 5, 394-402.
102. H.-L. Gao, N.-N. Wang, W.-M. Wang, H.-Y. Shen, X.-P. Zhou, Y.-X. Chang, R.-X. Zhang and J.-Z. Cui, Fine-tuning the magnetocaloric effect and SMMs behaviors of coplanar RE₄ complexes by β-diketonate coligands, *Inorg. Chem. Front.*, 2017, **4**, 860-870.
103. J. Wu, X.-L. Li, L. Zhao, M. Guo and J. Tang, Enhancement of Magnetocaloric Effect through Fixation of Carbon Dioxide: Molecular Assembly from Ln₄ to Ln₄ Cluster Pairs, *Inorg. Chem.*, 2017, **56**, 4104-4111.

104. X.-M. Luo, Z.-B. Hu, Q.-f. Lin, W. Cheng, J.-P. Cao, C.-H. Cui, H. Mei, Y. Song and Y. Xu, Exploring the Performance Improvement of Magnetocaloric Effect Based Gd-Exclusive Cluster Gd₆₀, *J. Am. Chem. Soc.*, 2018, **140**, 11219-11222.
105. J.-B. Peng, X.-J. Kong, Q.-C. Zhang, M. Orendáč, J. Prokleška, Y.-P. Ren, L.-S. Long, Z. Zheng and L.-S. Zheng, Beauty, Symmetry, and Magnetocaloric Effect—Four-Shell Keplerates with 104 Lanthanide Atoms, *J. Am. Chem. Soc.*, 2014, **136**, 17938-17941.
106. S.-D. Han, X.-H. Miao, S.-J. Liu and X.-H. Bu, Magnetocaloric effect and slow magnetic relaxation in two dense (3,12)-connected lanthanide complexes, *Inorg. Chem. Front.*, 2014, **1**, 549-552.
107. W.-M. Wang, X.-Z. Li, L. Zhang, J.-L. Chen, J.-H. Wang, Z.-L. Wu and J.-Z. Cui, A series of [2 × 2] square grid Ln^{III}₄ clusters: a large magnetocaloric effect and single-molecule-magnet behavior, *New J. Chem.*, 2019, **43**, 7419-7426.
108. W.-M. Wang, Z.-L. Wu, Y.-X. Zhang, H.-Y. Wei, H.-L. Gao and J.-Z. Cui, Self-assembly of tetra-nuclear lanthanide clusters via atmospheric CO₂ fixation: interesting solvent-induced structures and magnetic relaxation conversions, *Inorg. Chem. Front.*, 2018, **5**, 2346-2354.
109. W.-M. Wang, M.-J. Wang, S.-S. Hao, Q.-Y. Shen, M.-L. Wang, Q.-L. Liu, X.-F. Guan, X.-T. Zhang and Z.-L. Wu, ‘Windmill’-shaped Ln^{III}₄ (Ln^{III} = Gd and Dy) clusters: magnetocaloric effect and single-molecule-magnet behavior, *New J. Chem.*, 2020, **44**, 4631-4638.
110. W.-M. Wang, L.-Y. He, X.-X. Wang, Y. Shi, Z.-L. Wu and J.-Z. Cui, Linear-shaped Ln^{III}₄ and Ln^{III}₆ clusters constructed by a polydentate Schiff base ligand and a β-diketone

- co-ligand: structures, fluorescence properties, magnetic refrigeration and single-molecule magnet behavior, *Dalton Trans.*, 2019, **48**, 16744-16755.
111. A. Rasamsetty, C. Das, E. C. Sañudo, M. Shanmugam and V. Baskar, Effect of coordination geometry on the magnetic properties of a series of Ln₂ and Ln₄ hydroxo clusters, *Dalton Trans.*, 2018, **47**, 1726-1738.
112. H.-L. Gao, X.-P. Zhou, Y.-X. Bi, H.-Y. Shen, W.-M. Wang, N.-N. Wang, Y.-X. Chang, R.-X. Zhang and J.-Z. Cui, A Dy₄ single-molecule magnet and its Gd(iii), Tb(iii), Ho(iii), and Er(iii) analogues encapsulated by an 8-hydroxyquinoline Schiff base derivative and β-diketonate coligand, *Dalton Trans.*, 2017, **46**, 4669-4677.
113. A. K. Mondal, H. S. Jena, A. Malviya and S. Konar, Lanthanide-Directed Fabrication of Four Tetranuclear Quadruple Stranded Helicates Showing Magnetic Refrigeration and Slow Magnetic Relaxation, *Inorg. Chem.*, 2016, **55**, 5237-5244.
114. W.-M. Wang, L. Zhang, X.-Z. Li, L.-Y. He, X.-X. Wang, Y. Shi, J. Wang, J. Dong and Z.-L. Wu, Structures, fluorescence properties and magnetic properties of a series of rhombus-shaped Ln^{III}₄ clusters: magnetocaloric effect and single-molecule-magnet behavior, *New J. Chem.*, 2019, **43**, 12941-12949.
115. H. Yu, J.-X. Yang, J.-Q. Han, P.-F. Li, Y.-L. Hou, W.-M. Wang and M. Fang, Tetranuclear lanthanide complexes showing magnetic refrigeration and single molecule magnet behavior, *New J. Chem.*, 2019, **43**, 8067-8074.
116. D. I. Alexandropoulos, K. R. Vignesh, B. S. Dolinar and K. R. Dunbar, End-to-end azides as bridging ligands in lanthanide coordination chemistry: Magnetic and magnetocaloric properties of tetranuclear Ln₄ (Ln = Gd, Dy) complexes exhibiting a rare rhombus topology, *Polyhedron*, 2018, **151**, 255-263.

117. Y.-C. Zhang, Q.-L. Wang, G. Chen, P.-F. Shi and W.-M. Wang, Two linear-shaped Gd₄ clusters based on a multidentate ligand: Synthesis, structures, and magnetic refrigeration, *Polyhedron*, 2019, **169**, 247-252.
118. W.-M. Wang, T.-L. Han, Y.-L. Shao, X.-Y. Qiao, Z.-L. Wu, Q.-L. Wang, P. F. Shi, H.-L. Gao and J.-Z. Cui, Butterfly-shaped tetranuclear Ln₄ clusters showing magnetic refrigeration and single molecule-magnet behavior, *New J. Chem.*, 2018, **42**, 14949-14955.
119. Y.-X. Zhang, Y.-H. Zhang, B.-Y. Liu, W.-M. Wang, G.-P. Tang, H.-Y. Wei and Z.-L. Wu, Synthesis, luminescence and magnetic properties of tetranuclear lanthanide-based (Eu₄, Gd₄ and Dy₄) clusters, *New J. Chem.*, 2018, **42**, 18305-18311.
120. Y.-X. Zhang, M. Li, B.-Y. Liu, Z.-L. Wu, H.-Y. Wei and W.-M. Wang, A series of planar tetranuclear lanthanide complexes: axial ligand modulated magnetic dynamics in Dy₄ species, *RSC Advances*, 2017, **7**, 55523-55535.
121. S. Biswas, A. K. Mondal and S. Konar, Densely Packed Lanthanide Cubane Based 3D Metal–Organic Frameworks for Efficient Magnetic Refrigeration and Slow Magnetic Relaxation, *Inorg. Chem.*, 2016, **55**, 2085-2090.
122. B.-L. Liu, Q.-F. Xu, L.-S. Long and L.-S. Zheng, A Gd-based borate–carbonate framework exhibiting a large magnetocaloric effect at a low magnetic field, *Dalton Trans.*, 2021, **50**, 12831-12834.
123. P.-E. Car, M. Perfetti, M. Mannini, A. Favre, A. Caneschi and R. Sessoli, Giant field dependence of the low temperature relaxation of the magnetization in a dysprosium(iii)–DOTA complex, *Chem. Commun.*, 2011, **47**, 3751-3753.

124. A. Abragam and B. Bleaney, *Electron Paramagnetic Resonance of Transition Ions*, Clarendon Press, Oxford, 1970. 102. A. Singh and K. N. Shrivastava, Optical-acoustic two-phonon relaxation in spin systems, *phys. status solidi (b)*, 1979, **95**, 273-277.
125. K. N. Shrivastava, Theory of Spin–Lattice Relaxation, *phys. status solidi (b)*, 1983, **117**, 437-458.
126. P. Evans, D. Reta, G. F. S. Whitehead, N. F. Chilton and D. P. Mills, Bis-Monophospholyl Dysprosium Cation Showing Magnetic Hysteresis at 48 K, *J. Am. Chem. Soc.*, 2019, **141**, 19935-19940.
127. D. Reta and N. F. Chilton, Uncertainty estimates for magnetic relaxation times and magnetic relaxation parameters, *Phys. Chem. Chem. Phys.*, 2019, **21**, 23567-23575.
128. A. Swain, R. Martin, K. R. Vignesh, G. Rajaraman, K. S. Murray and S. K. Langley, Enhancing the barrier height for magnetization reversal in 4d/4f $\text{Ru}^{\text{II}}_2\text{Ln}^{\text{III}}_2$ “butterfly” single molecule magnets (Ln = Gd, Dy) via targeted structural alterations, *Dalton Trans.*, 2021, **50**, 12265-12274.
129. S. Saha, K. S. Das, T. Sharma, S. Bala, A. Adhikary, G.-Z. Huang, M.-L. Tong, A. Ghosh, B. Das, G. Rajaraman and R. Mondal, Synergistic Experimental and Theoretical Studies of Luminescent–Magnetic Ln_2Zn_6 Clusters, *Inorg. Chem.*, 2022, **61**, 2141-2153.
130. T. Rajeshkumar, H. V. Annadata, M. Evangelisti, S. K. Langley, N. F. Chilton, K. S. Murray and G. Rajaraman, Theoretical Studies on Polynuclear $\{\text{Cu}^{\text{II}}_5\text{Gd}^{\text{III}}_n\}$ Clusters (n = 4, 2): Towards Understanding Their Large Magnetocaloric Effect, *Inorg. Chem.*, 2015, **54**, 1661-1670.
131. T. Rajeshkumar, R. Jose, P. R. Remya and G. Rajaraman, Theoretical Studies on Trinuclear $\{\text{Mn}^{\text{III}}_2\text{Gd}^{\text{III}}\}$ and Tetranuclear $\{\text{Mn}^{\text{III}}_2\text{Gd}^{\text{III}}_2\}$ Clusters: Magnetic Exchange,

- Mechanism of Magnetic Coupling, Magnetocaloric Effect, and Magneto–Structural Correlations, *Inorg. Chem.*, 2019, **58**, 11927-11940.
132. S. K. Singh, T. Rajeshkumar, V. Chandrasekhar and G. Rajaraman, Theoretical studies on {3d-Gd} and {3d-Gd-3d} complexes: Effect of metal substitution on the effective exchange interaction, *Polyhedron*, 2013, **66**, 81-86.
133. E. Cremades, S. Gómez-Coca, D. Aravena, S. Alvarez and E. Ruiz, Theoretical Study of Exchange Coupling in 3d-Gd Complexes: Large Magnetocaloric Effect Systems, *J. Am. Chem. Soc.*, 2012, **134**, 10532-10542.
134. T. N. Hooper, S. K. Langley, S. Gómez-Coca, G. Lorusso, E. Ruiz, K. S. Murray, M. Evangelisti and E. K. Brechin, Coming full circle: constructing a [Gd₆] wheel dimer by dimer and the importance of spin topology, *Dalton Trans.*, 2017, **46**, 10255-10263.
135. T. Rajeshkumar, S. K. Singh and G. Rajaraman, A computational perspective on magnetic coupling, magneto-structural correlations and magneto-caloric effect of a ferromagnetically coupled {Gd^{III}–Gd^{III}} Pair, *Polyhedron*, 2013, **52**, 1299-1305.
136. S. Mukherjee, J. Lu, G. Velmurugan, S. Singh, G. Rajaraman, J. Tang and S. K. Ghosh, Influence of Tuned Linker Functionality on Modulation of Magnetic Properties and Relaxation Dynamics in a Family of Six Isotypic Ln₂ (Ln = Dy and Gd) Complexes, *Inorg. Chem.*, 2016, **55**, 11283-11298.
137. T. Gupta and G. Rajaraman, Modelling spin Hamiltonian parameters of molecular nanomagnets, *Chem. Commun.*, 2016, **52**, 8972-9008.
138. S. Roy, P. Shukla, P. Prakash Sahu, Y.-C. Sun, N. Ahmed, S. Chandra Sahoo, X.-Y. Wang, S. Kumar Singh and S. Das, Zero-field Slow Magnetic Relaxation Behavior of

- Dy₂ in a Series of Dinuclear {Ln₂} (Ln=Dy, Tb, Gd and Er) Complexes: A Combined Experimental and Theoretical Study, *Eur. J. Inorg. Chem.*, 2022, **2022**, e202100983.
139. Y.-C. Chen, J.-L. Liu, L. Ungur, J. Liu, Q.-W. Li, L.-F. Wang, Z.-P. Ni, L. F. Chibotaru, X.-M. Chen and M.-L. Tong, Symmetry-Supported Magnetic Blocking at 20 K in Pentagonal Bipyramidal Dy(III) Single-Ion Magnets, *J. Am. Chem. Soc.*, 2016, **138**, 2829–2837.
140. J. Liu, Y.-C. Chen, J.-L. Liu, V. Vieru, L. Ungur, J.-H. Jia, L. F. Chibotaru, Y. Lan, W. Wernsdorfer, S. Gao, X.-M. Chen and M.-L. Tong, A Stable Pentagonal Bipyramidal Dy(III) Single-Ion Magnet with a Record Magnetization Reversal Barrier over 1000 K, *J. Am. Chem. Soc.*, 2016, **138**, 5441–5450.
141. A. B. Canaj, S. Dey, E. R. Martí, C. Wilson, G. Rajaraman and M. Murrie, Insight into D_{6h} Symmetry: Targeting Strong Axiality in Stable Dysprosium(III) Hexagonal Bipyramidal Single-Ion Magnets, *Angew. Chem. Int. Ed.*, 2019, **58**, 14146–14151.
142. Z. Zhu, C. Zhao, T. Feng, X. Liu, X. Ying, X.-L. Li, Y.-Q. Zhang and J. Tang, Air-Stable Chiral Single-Molecule Magnets with Record Anisotropy Barrier Exceeding 1800 K, *J. Am. Chem. Soc.*, 2021, **143**, 10077–10082.
143. V. S. Parmar, F. Ortu, X. Ma, N. F. Chilton, R. Clérac, D. P. Mills and R. E. P. Winpenny, Probing Relaxation Dynamics in Five-Coordinate Dysprosium Single-Molecule Magnets, *Chem. Eur. J.*, 2020, **26**, 7774–7778.
144. M. Gregson, N. F. Chilton, A.-M. Ariciu, F. Tuna, I. F. Crowe, W. Lewis, A. J. Blake, D. Collison, E. J. L. McInnes, R. E. P. Winpenny and S. T. Liddle, A monometallic lanthanide bis (methanediide) single molecule magnet with a large energy barrier and complex spin relaxation behaviour, *Chem. Sci.*, 2015, **7**, 155–165.

145. X.-L. Ding, Y.-Q. Zhai, T. Han, W.-P. Chen, Y.-S. Ding and Y.-Z. Zheng, A Local D_{4h} Symmetric Dysprosium(III) Single-Molecule Magnet with an Energy Barrier Exceeding 2000 K, *Chem. Eur. J.*, 2021, **27**, 2623–2627.
146. S. Demir, M. I. Gonzalez, L. E. Darago, W. J. Evans and J. R. Long, Giant coercivity and high magnetic blocking temperatures for N_2^{3-} radical-bridged dilanthanide complexes upon ligand dissociation, *Nat Commun.*, 2017, **8**, 2144.